JOURNAL OF GEOPHYSICAL RESEARCH, VOL. 113, C11012, doi:10.1029/2008JC004783, 2008

Click Here for Full Article

Variability of sea ice simulations assessed with RGPS kinematics

R. Kwok,[1] E. C. Hunke,[2] W. Maslowski,[3] D. Menemenlis,[1] and J. Zhang[4]

Received 25 February 2008; revised 21 July 2008; accepted 19 August 2008; published 12 November 2008.

[1] Sea ice drift and deformation from coupled ice-ocean models are compared with high-resolution ice motion from the RADARSAT Geophysical Processor System (RGPS). In contrast to buoy drift, the density and extent of the RGPS coverage allows a more extensive assessment and understanding of model simulations at spatial scales from ~10 km to near basin scales and from days to seasonal timescales. This work illustrates the strengths of the RGPS data set as a basis for examining model ice drift and its gradients. As it is not our intent to assess relative performance, we have selected four models with a range of attributes and grid resolution. Model fields are examined in terms of ice drift, export, deformation, deformation-related ice production, and spatial deformation patterns. Even though the models are capable of reproducing large-scale drift patterns, variability among model behavior is high. When compared to the RGPS kinematics, the characteristics shared by the models are (1) ice drift along coastal Alaska and Siberia is slower, (2) the skill in explaining the time series of regional divergence of the ice cover is poor, and (3) the deformation-related volume production is consistently lower. Attribution of some of these features to specific causes is beyond our current scope because of the complex interplay between model processes, parameters, and forcing. The present work suggests that high-resolution ice drift observations, like those from the RGPS, would be essential for future model developments, improvements, intercomparisons, and especially for evaluation of the small-scale behavior of models with finer grid spacing.

Citation: Kwok, R., E. C. Hunke, W. Maslowski, D. Menemenlis, and J. Zhang (2008), Variability of sea ice simulations assessed with RGPS kinematics, *J. Geophys. Res.*, *113*, C11012, doi:10.1029/2008JC004783.

1. Introduction

[2] Sea ice is a floating, solid medium that controls the complex exchanges of momentum, heat, and mass between the sea and the atmosphere over the polar oceans. Its existence is in turn dependent on the thermodynamic and dynamic states of these two bounding geophysical fluids. Thus, models of sea ice are an important component in the implementation of any numerical model that attempts to understand the role of the polar regions in global climate. Sea ice responds to forcings over a broad range of spatial and temporal length scales. While the large-scale circulation of sea ice determines the advective part of the ice balance, the shorter length scales are especially important because the response of sea ice to gradients in forcings and to boundary conditions is concentrated along narrow fractures and cracks. Exposed open water associated with mechanical failure of the ice cover controls the abundance of thin ice and the many surface processes dependent on thin ice, such as turbulent heat flux to the atmosphere. The broad temporal and spatial spectra of sea ice motion present a particular challenge to observational systems and model simulations.

[3] An accurate ice dynamics model for climate studies must reflect the appropriate expressions of the large- and small-scale processes (e.g., openings/closings) and the states of the ice cover in terms of its area and thickness distribution. Differentiation of openings and closings is important because of how they impact the ice thickness distribution and ice strength. Extensive assessments of sea ice simulations have always been limited by the availability of observational data with appropriate spatial and temporal timescales. Buoy drifts have produced useful insights into model performance [e.g., *Meier and Maslanik*, 2003; *Zhang et al.*, 2003]. However, even though buoy observations can provide unparalleled temporal sampling of drift tracks, their spatial separation (typically hundreds of kilometers except for dedicated field campaigns) and their preferential deployment over thicker ice have confined their effectiveness to providing model assessment only at relatively large length scales. Estimates of divergence and convergence from gradients in buoy drift represent only large-scale sums of openings and closings and are therefore not very useful for understanding smaller-scale model behavior. The uncertainties in ice drift from moderate-resolution satellite observations (order of km d^{-1}), while useful for examining large-scale circulation [*Martin and Gerdes*, 2007], are still

[1]Jet Propulsion Laboratory, California Institute of Technology, Pasadena, California, USA.
[2]Climate, Ocean, and Sea Ice Modeling Program, Los Alamos National Laboratory, Los Alamos, New Mexico, USA.
[3]Department of Oceanography, Graduate School of Engineering and Applied Sciences, Naval Postgraduate School, Monterey, California, USA.
[4]Polar Science Center, Applied Physics Laboratory, College of Ocean and Fishery Sciences, University of Washington, Seattle, Washington, USA.

Copyright 2008 by the American Geophysical Union.
0148-0227/08/2008JC004783$09.00

Table 1. Four Models in This Assessment[a]

Model	Grid Resolution (km)	Ice Dynamics	Yield Curve	Ice Strength	Ocean Model	Atmospheric Forcing
University of Washington (PIOMAS) B-Grid	22	VP	teardrop	see *Rothrock* [1975]	POP	NCEP-NCAR
Jet Propulsion Laboratory (ECCO2) C-Grid	18	VP	ellipse	$P^* = 2.75 \times 10^4$ N m^{-2}	MITgcm	NCEP-NCAR
NPS B-Grid	9	VP	ellipse	$P^* = 2.75 \times 10^4$ N m^{-2}	POP	ECMWF
LANL B-Grid	40	EVP	ellipse	see *Rothrock* [1975]	POP[b]	see *Hunke and Holland* [2007]

[a]PIOMAS, Pan-Arctic Ice-Ocean Modeling and Assimilation System; VP, viscous-plastic; POP, Parallel Ocean Program; NCEP, National Centers for Environmental Prediction; NCAR, National Center for Atmospheric Research; ECCO2, Estimating the Circulation and Climate of the Ocean, Phase II project; MITgcm, Massachusetts Institute of Technology general circulation model; NPS, Naval Postgraduate School; ECMWF, European Centre for Medium-Range Weather Forecasts; LANL, Los Alamos National Laboratory; EVP, elastic-viscous-plastic.

[b]POP output from a prior simulation is used to force the stand-alone ice simulations in the LANL case.

too high for fine-scale ice drift associated with fractures/cracks or openings and closings in the ice cover.

[4] Only with sea ice kinematics derived from high-resolution SAR imagery have we been able to approach the spatial length scale required to resolve these processes [*Kwok et al.*, 1995]. Launched in November 1996, RADARSAT, with its wide-swath imaging mode, has provided routine near basin-scale coverage of the Arctic Ocean at high resolution (~100 m). The fine-scale sea ice kinematics produced by the RADARSAT Geophysical Processor System (RGPS) [*Kwok*, 1998] resolve fracture patterns and offer a level of spatial and temporal detail that allows for a closer examination of small-scale deformation of the ice cover within a near basin-scale context. Dense 3-day ice trajectories (~10 km sample spacing) over six winters (1997–2002) are now available. These products have been used to drive a granular model of sea ice [*Hopkins et al.*, 1999] and a single-column ice thickness model [*Curry et al.*, 2001]. The strain rates have also been used in a study relating Arctic pack ice stress and deformation [*Richter-Menge et al.*, 2002] and in a study of rafting and redistribution of ice thickness [*Babko et al.*, 2002]. The ice motion data are being used in a data fusion study to derive the best estimate of ice deformation near SHEBA [*Lindsay*, 2002]. *Coon et al.* [1998], *Hibler* [2001], and *Hibler and Schulson* [2000] have used the RGPS deformation patterns to understand the implications of modeling an anisotropic ice cover. One collection of papers on small-scale kinematics and dynamics includes one by *Kwok and Coon* [2006].

[5] The objective of this paper is to illustrate the strengths of the RGPS data set as a basis for examining model ice drift and its gradients at different spatial and temporal scales. This adds to the work of *Lindsay et al.* [2003] who investigated some aspects of using RGPS to examine the simulation results from one particular model. This paper is not about model intercomparison; we avoid direct comparisons between models. We have selected four models with very different attributes; the assessment approaches are intended to show the variability in behavior of the four models when compared to RGPS observations. Arctic Ocean sea ice results are from models based at: the University of Washington (PIOMAS), Jet Propulsion Laboratory (ECCO2), Naval Postgraduate School (NPS), and Los Alamos National Laboratory (LANL).

[6] This paper is organized as follows. Section 2 describes the attributes of the four models, the RGPS observations, and the ancillary data sets used in our analyses. In particular, the special characteristics of the high-resolution RGPS ice motion are discussed. In Section 3, model ice drifts are compared with buoy and RGPS observations, and satellite and model-derived ice area outflows at the Fram Strait are contrasted. Section 4 examines differences in the regional deformation obtained from model and RGPS ice drift. Correlations between the model and RGPS estimates are calculated. Variability in the deformation-related ice production is estimated and discussed in Section 5. Section 6 shows examples where there are correspondences between deformation patterns in the model fields and the linear kinematic features from RGPS data set. The last section summarizes the paper.

2. Model and Data Descriptions

[7] In this section, we provide a brief description of the characteristics of the four models (Table 1), the RGPS observations, and the ancillary data sets used here. Daily fields of model ice drift are used in the assessments in the following sections.

2.1. Four Models

2.1.1. Pan-Arctic Ice-Ocean Modeling and Assimilation System

[8] PIOMAS (Pan-Arctic Ice-Ocean Modeling and Assimilation System) is a coupled parallel ocean and sea ice model. It consists of the thickness and enthalpy distribution (TED) sea ice model [*Zhang and Rothrock*, 2001, 2003] and the Parallel Ocean Program (POP) developed at Los Alamos National Laboratory. The TED sea ice model is a dynamic thermodynamic model that also explicitly simulates ice ridging. It has 12 categories each for ice thickness, ice enthalpy, and snow. It employs a teardrop viscous-plastic rheology [*Zhang and Rothrock*, 2005], a mechanical redistribution function that determines ice ridging [*Thorndike et al.*, 1975; *Rothrock*, 1975; *Hibler*, 1980], and a line successive relaxation (LSR) scheme to solve the ice momentum equation [*Zhang and Hibler*, 1997]. PIOMAS is configured to cover the region north of 43°N. The model grid is based on a generalized orthogonal curvilinear coordinate system with the northern grid pole displaced into Greenland. The mean horizontal resolution is 22 km for the Arctic, Barents, and GIN (Greenland-Iceland-Norwegian) seas, and Baffin Bay. The model is one-way nested to a similar but global ice-ocean model [*Zhang*, 2007]. Daily satellite ice concentration data (data are available at http://polar.ncep.noaa.gov/seaice/Analyses.html) are assimilated in PIOMAS following *Lindsay and Zhang* [2006]. Ice drift is not assimilated.

2.1.2. Estimating the Circulation and Climate of the Ocean, Phase II Project

[9] The sea ice fields provided by the Estimating the Circulation and Climate of the Ocean, Phase II project (ECCO2) are from a global ocean and sea ice simulation carried out using the Massachusetts Institute of Technology general circulation model (MITgcm) [*Marshall et al.*, 1997]. This particular ECCO2 simulation, a baseline integration labeled cube37, has not yet been constrained by oceanic and sea ice data. The model configuration is described by *Menemenlis et al.* [2005]. A cube-sphere grid projection is employed, which permits relatively even grid spacing throughout the domain and which avoids polar singularities [*Adcroft et al.*, 2004]. Each face of the cube comprises 510 by 510 grid cells for a mean horizontal grid spacing of 18 km. The model is integrated in a volume-conserving configuration using a finite volume discretization with C-grid staggering of the prognostic variables. The ocean model is coupled to a sea ice model that uses a two-category, zero-layer thermodynamic model to compute sea ice thickness and concentration [*Hibler*, 1980]. Ice mechanics follow the viscous plastic rheology of *Hibler* [1979] and the ice momentum equation is solved numerically using a C-grid implementation (M. Losch et al., A dynamic-thermodynamic sea ice model on an Arakawa C-grid for coupled ocean sea/ice estimation, submitted to *Journal of Geophysical Research*, 2008) of the line successive relaxation (LSR) dynamics model of *Zhang and Hibler* [1997]. Snow cover is simulated as per *Zhang et al.* [1998]. Open water, dry ice, wet ice, dry snow, and wet snow albedo are, respectively, 0.15, 0.85, 0.76, 0.94, and 0.8. This particular ECCO2 simulation is initialized from rest using the January temperature and salinity distribution from the paper by *Conkright et al.* [2002] (hereinafter referred to as WOA01) and it is integrated for 32 years prior to the 1996–2001 period discussed in this study. Surface boundary conditions are from the National Centers for Environmental Prediction and the National Center for Atmospheric Research (NCEP-NCAR) atmospheric reanalysis [*Kistler et al.*, 2001]. Six-hourly surface winds, temperature, humidity, downward short- and long-wave radiations, and precipitation are converted to heat, freshwater, and wind stress fluxes using the *Large and Pond* [1981, 1982] bulk formulae. Shortwave radiation decays exponentially as per *Paulson and Simpson* [1977]. Additionally the time-mean river runoff from *Large and Nurser* [2001] is applied near the coastline and, where there is open water, there is a relaxation to monthly mean WOA01 sea surface salinity with a time constant of 45 days. Further details can be found in the papers by *Menemenlis et al.* [2005] and *Fox-Kemper and Menemenlis* [2008] (see also http://ecco2.org/).

2.1.3. NPS

[10] The NPS regional model used for analysis in this study [*Maslowski et al.*, 2004] consists of the Los Alamos National Laboratory (LANL) Parallel Ocean Program (POP) model with a free surface formulation [*Dukowicz and Smith*, 1994] coupled to a Hibler-type sea ice model [*Hibler*, 1979; *Zhang and Hibler*, 1997] with a viscous-plastic rheology, the zero-layer approximation of heat conduction through ice and a simplified surface energy budget [*Zhang et al.*, 1999; *Maslowski and Lipscomb*, 2003]. Both components of the coupled model use identical rotated spherical coordinate grids to eliminate a singularity at the pole and to simplify the coupling between the models. The grid is configured at 1/12° (~9 km) in the horizontal and 45 fixed depth layers in the vertical direction. The pan-Arctic model domain includes all the sea ice covered oceans and marginal seas of the northern hemisphere. Multidecade simulations have been completed, including 48-year spin-up and four 1979–2004 interannual runs forced with realistic daily averaged atmospheric data, including the ECMWF 1979–1993 reanalysis (ERA15) and 1994–2004 operational products [*Maslowski et al.*, 2007]. Daily snapshots of sea ice output from one of the interannual runs are used in this paper.

[11] The sea ice model that produced the results used here employs a simplified representation of sea ice thermodynamics and strength parameterization compared to the other three models [*Maslowski and Lipscomb*, 2003]. In particular, a more sophisticated representation of the ice thickness using multiple categories of sea ice and of ice strength based on the amount and thickness of thin ice fraction allows significant improvements in modeled ice drift and deformation in more recent models. Such limitations are in a major part responsible for the results described in this paper when the performance of this model is compared to the RGPS data set. Another, perhaps less important factor is the difference between ECMWF atmospheric forcing data used in the NPS model and NCEP-NCAR-based data used in the other three models (Table 1). A combination of high-resolution and improved parameterizations of sea ice thermodynamics and ice strength produces much more realistic simulations in the currently used model at NPS [*Maslowski and Lipscomb*, 2003]. However, results from the new model integration for the time period of the RGPS data are not available at the time of this work.

2.1.4. LANL

[12] The LANL simulation employs the sea ice model by *Hunke and Lipscomb* [2006], and is intended to be representative of sea ice simulations within current state-of-the-art global climate models. The model is configured for the 1°, displaced pole grid used for the ocean and ice components of the fully coupled Community Climate System Model (CCSM) by *Collins et al.* [2006], and output from the CCSM ocean component (POP) in a fully coupled CCSM run is used for the lower boundary conditions in CICE, including sea surface temperature and salinity, surface currents and a deep ocean heat flux. The sea surface temperature is modified on the basis of applied atmospheric forcing and the sea ice response using a thermodynamic ocean mixed layer parameterization within CICE.

[13] The atmospheric forcing used for this run (1980–2004) is a modified version of the *Large and Yeager* [2004] data set described by *Hunke and Holland* [2007]. A stability-based atmospheric boundary layer formulation is used to compute the turbulent sensible and latent heat fluxes and wind stress components as described by *Hunke and Lipscomb* [2006]. CICE features the elastic-viscous-plastic dynamics module of *Hunke and Dukowicz* [2002], advection via incremental remapping as in the paper by *Lipscomb and Hunke* [2004], the energy-conserving approach to ice thermodynamics of *Bitz and Lipscomb* [1999], and a five-category ice thickness distribution, with four ice layers and one snow layer in each category. State variables include ice

area and surface temperature for each thickness category, and ice or snow volume and enthalpy for each layer within each thickness category. Transformations of state variables among thickness categories are also performed using an incremental remapping algorithm [*Lipscomb*, 2001]; ice ridging and rafting are modeled using an energy-based parameterization for mechanical redistribution [*Lipscomb et al.*, 2007]. The sea ice albedo follows the dual-band, thickness- and temperature-dependent formulation of CCSM. The grid spacing ranges between 20 and 85 km, averaging 40 km north of 70 N. Other than not being coupled to an active ocean model, the sea ice model configuration and initialization is identical to the 1° case of *Hunke and Holland* [2007].

2.2. RGPS Data Set

[14] Since November of 1996, the RADARSAT imaging radar has provided routine high-resolution SAR mappings of the western Arctic Ocean at ~3-day intervals. The sampling period of ~3 days is determined by available data allocation even though a shorter sampling interval would be more optimal for resolving small-scale kinematics. Acquired radar data are recorded and processed at the Alaska Satellite Facility (ASF) in Fairbanks, Alaska. The resultant sea ice imagery is analyzed by procedures implemented in the RADARSAT Geophysical Processor System (RGPS). Primary estimates from the RGPS are arrays of sea ice trajectories starting from an initial uniformly spaced grid of ~10 km. *Lindsay and Stern* [2003] report that the median magnitude of displacement differences between buoy drift (via ARGOS positioning) and RGPS motion estimates is 323 m. The uncertainty in RGPS displacements is comparable to those from drifting buoys. Secondary procedures in the RGPS derive estimates of deformation, histogram of thin ice thickness, and multiyear ice coverage from the record of time-varying backscatter and cell areas computed on the deforming Lagrangian grid cells. Line segments connecting the grid points define cells within which these quantities are computed. The ice thickness histogram is of seasonal ice grown in openings during the winter. Details of the analysis procedures can be found in the papers by *Kwok et al.* [1995] and *Kwok and Cunningham* [2002]. A brief summary of the seasonal ice growth calculations is provided in Section 5.

[15] The RGPS data set used here consists of products from six winters (1996–1997, 1997–1998, 1998–1999, 1999–2000, 2000–2001, and 2001–2002). Winters span the period between October and May. Gaps in the ice motion data sets are due to the lack of backscatter contrast for tracking ice features in the SAR imagery. Of the full set of RGPS products, three are used here: ice motion, deformation, and ice thickness histogram. The ice deformation product contains the geographic location, area, and velocity gradients at each cell computed at every time step. Nominal time step is typically ~3 days. Seasonal ice production is from the record of the derived thickness estimates at Lagrangian cells stored in the ice thickness histogram product.

[16] Measures of sea ice deformation of the Arctic Ocean used in the comparison model and RGPS data are divergence, vorticity, and shear computed at different length scales. In the following analysis, the divergence, vorticity, and shear of a given area (Lagrangian cell or region) are written as:

$$\nabla \cdot u = u_x + v_y, \quad \zeta = v_x - u_y, \quad e = \left[(u_x - v_y)^2 + (u_y + v_x)^2 \right]^{\frac{1}{2}} \tag{1}$$

where u_x, u_y, v_x, and v_y are the spatial gradients in ice motion computed using a line integral around the boundary of that area, vis.:

$$u_x = \frac{1}{A} \oint u dy \qquad u_y = -\frac{1}{A} \oint u dx \qquad v_x = \frac{1}{A} \oint v dy$$
$$v_y = -\frac{1}{A} \oint v dx \tag{2}$$

The line segments connecting the vertices of a polygon (or grid cell in this case) define the regional boundaries. In our case, the smallest area is that defined by the boundaries of a RGPS cell (~10 km on a side). $\nabla \cdot u$ is a measure of the rate of area change, ζ is the principal measure of rotation rate, and e is the scalar magnitude of shear. The procedure used to evaluate these integrals is shown in the Appendix A.

2.3. Common Projection

[17] All daily model scalar and vector fields are mapped onto an Earth-fixed Cartesian grid using a polar stereographic projection. This transformation maps the Earth's surface to a plane parallel to 70°N. The origin is at the pole and the positive x axis runs along 45°E. The mapping is conformal, i.e., angles are preserved. The scale is 1.0 at 70°N and 0.97 at the pole. All ice motion vectors are scaled consistently when they are converted to this planimetric representation.

3. Ice Drift and Fram Export

[18] This section compares ice drift and ice area export at Fram Strait from model simulations with those from buoys and RGPS observations. While the buoy and RGPS drifts allow us to contrast the model behavior at different temporal scales, we show that the coverage of the RGPS data provides a more comprehensive spatial depiction of the differences between model and data.

3.1. Simulated Thickness Fields

[19] In general, the response of the ice cover to external forcing is dependent on ice strength that is in turn dependent on ice thickness. Therefore, the simulated thickness fields (shown in Figure 1) are of interest because they are useful for interpreting the results of our assessment of the model drifts throughout this paper. Except for the NPS fields, the spatial character of the modeled thickness distributions does not vary significantly during the winters bracketed by the two January fields (1997 and 2001) shown. The expected thickness gradient across the Arctic Ocean with the thickest ice north of Greenland and thinner ice toward the Siberian coast is seen in all the fields. Temporally, the NPS fields show a noticeable negative trend in mean ice thickness compared to the others (starting at ~3.0 m and ending at ~2.2 m (the fields of the intervening years are not shown)). Their results are further discussed by *Maslowski et al.*

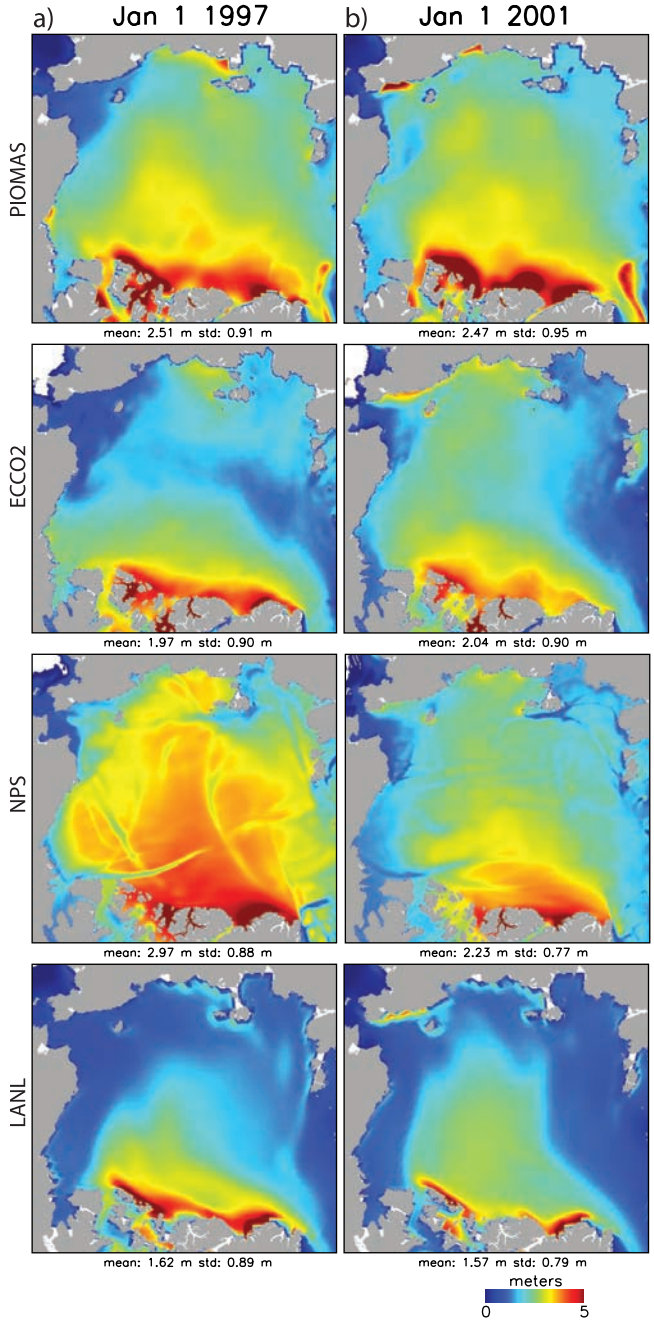

Figure 1. Simulated thickness fields. (a) 1 January 1997 and (b) 1 January 2001.

[2007] and *Stroeve and Maslowski* [2007]. The NPS fields also show what looks to be fracture patterns in the ice cover. In descending order, the mean thickness of the PIOMAS, ECCO2, and LANL fields are approximately 2.5 m, 2.0 m, and 1.6 m.

3.2. Comparison With Buoy Drift

[20] Prior to comparisons, daily model ice drifts are spatially interpolated to the buoy locations. Since the sampling of the 12-hour buoy drifts are aligned with daily model outputs, no temporal interpolation is necessary. Differences between daily model and buoy drifts are summarized in Table 2. To reduce noise when the model-buoy signals are low, differences are not computed when either the daily model or buoy displacement falls below 1 km. As a result, the number of model-data pairs (N) varies between models. These daily differences provide a measure of the simulated sea ice response to short-term wind forcing because the wind accounts for a large fraction of the daily ice drift [*Thorndike and Colony*, 1982]. While there is a range of performance in the model simulations, the metrics in Table 2 (mean/standard deviation of the differences in drift in the x and y directions, mean/standard deviation of the directional differences, and the squared correlation between the two drift vectors) show that individual model behavior is at least internally consistent, i.e., they do not vary considerably from year to year. At this timescale, there are no noticeable biases in the mean motion. The squared correlation (ρ^2) between daily model and buoy drifts ranges from 0.2 to 0.8. The daily PIOMAS simulations are generally better (i.e., lower $\sigma_{\Delta x,\Delta y}$, $\sigma_{\Delta\theta}$ and higher ρ^2) perhaps because this model assimilates daily satellite ice concentrations. In the NPS comparisons, the higher ρ^2 during the last 3 years could be due to the thinner cover. It is interesting to note that, for two winters (October 1996 to April 1997 and October 2000 to May 2001), the daily drifts from the LANL model account for a far larger fraction of the variability of buoy drift ($\rho^2 = 0.77$ and 0.80) than the other models (those years also have the lowest $\sigma_{\Delta x,\Delta y}$). This better performance may be potentially attributable to the improved atmospheric forcing data used by the LANL model, discussed by *Hunke and Holland* [2007], but an in-depth analysis, although interesting, is beyond the scope of the present study.

3.3. Comparison With RGPS Ice Drift

[21] Instead of comparing daily ice drift, in this section we examine the variability in monthly displacements when compared with RGPS drift tracks. Whereas the daily drift comparisons provide a measure of the daily response to the wind, the monthly differences capture the longer-term coupled ice-ocean response of these models to the prescribed atmospheric forcing. As the sampling of the RGPS ice motion estimates are not uniform in time and space, we first align the two data sets by constructing model drift trajectories to simulate the observed RGPS drift tracks. The monthly model-based trajectories are created such that they share identical initial locations as the RGPS observations near the beginning of each month. The time of the last observation is defined by the last RGPS observation of that month. Gridded model motion fields are interpolated, bilinearly, to propagate the drift track on a daily basis. Each model track is defined by the same initial location and identical temporal extent. Even though modeled ice motion is expected to have fairly large spatial correlation length scales, i.e., smooth, it should be recognized that small errors introduced in this alignment process would reduce the model-RGPS correlation. The spatial density of the RGPS trajectories (sampled on an ~10 km grid) is much higher and thus there is 1 order of magnitude more trajectory pairs for sampling the spatial differences than using buoy drifts.

[22] Table 3 summarizes the differences between monthly model and RGPS ice drift for the winters (November through April) where data are available. Spatial differences, discussed later, are shown in Figure 2. The results in Table 3 show that the $\sigma_{\Delta x,\Delta y}$ are lower than those in Table 2.

Table 2. Differences Between Daily Model and Buoy Ice Drift[a]

	$m_{\Delta x}$	$\sigma_{\Delta x}$	$m_{\Delta y}$	$\sigma_{\Delta y}$	$m_{\Delta\theta}$	$\sigma_{\Delta\theta}$	ρ^2	N
			PIOMAS					
Oct 1996 to May 1997	−0.1	4.5	0.2	4.2	5.7	34.2	0.69	1995
Oct 1997 to May 1998	−0.6	4.8	1.1	5.0	9.2	41.5	0.62	2379
Oct 1998 to May 1999	−0.2	5.1	−0.4	5.1	12.3	39.5	0.57	1873
Oct 1999 to May 2000	0.6	4.3	−0.3	4.2	6.8	35.3	0.66	1794
Oct 2000 to May 2001	−0.3	4.5	0.5	4.3	5.3	32.7	0.69	2034
Oct 2001 to May 2002	−0.1	4.8	−0.1	5.2	6.6	41.5	0.62	2781
Oct 2002 to May 2003	−0.5	4.8	0.0	5.2	7.3	39.3	0.63	2506
Oct 2003 to May 2004	−0.5	4.6	0.5	4.5	8.2	36.2	0.67	2714
			ECCO2					
Oct 1996 to May 1997	0.0	7.8	0.1	6.7	−4.7	63.6	0.27	2257
Oct 1997 to May 1998	0.2	7.4	1.0	7.1	3.4	70.6	0.24	3034
Oct 1998 to May 1999	−0.5	7.9	0.5	7.0	−1.0	74.7	0.19	2384
Oct 1999 to May 2000	0.0	6.3	−0.3	6.2	−6.3	64.2	0.31	2053
Oct 2000 to May 2001	0.4	6.6	0.7	6.2	−6.9	62.7	0.34	2262
Oct 2001 to May 2002	0.3	7.3	−0.2	7.6	−1.5	70.8	0.24	3054
Oct 2002 to May 2003	0.1	7.9	−0.3	7.6	3.2	71.6	0.21	2982
Oct 2003 to May 2004	0.4	7.8	0.7	7.1	−3.6	68.6	0.22	3118
			NPS					
Oct 1996 to May 1997	1.5	6.0	0.4	6.2	7.0	55.0	0.35	759
Oct 1997 to May 1998	0.0	6.3	−0.4	7.1	3.1	81.4	0.13	935
Oct 1998 to May 1999	1.5	7.5	0.0	7.7	3.6	74.6	0.23	472
Oct 1999 to May 2000	−1.5	6.0	1.0	4.5	16.3	70.6	0.21	306
Oct 2000 to May 2001	−0.2	5.6	2.1	5.5	0.1	50.0	0.55	760
Oct 2001 to May 2002	−0.5	5.8	1.0	5.9	16.7	50.4	0.49	1377
Oct 2002 to May 2003	−0.6	5.8	−0.1	5.9	12.9	53.7	0.47	1669
			LANL					
Oct 1996 to May 1997	0.4	3.2	−0.5	3.3	10.8	21.4	0.80	2688
Oct 1997 to May 1998	0.2	5.9	0.5	6.3	7.9	56.5	0.41	3188
Oct 1998 to May 1999	0.1	6.2	0.1	5.6	5.1	53.9	0.39	2470
Oct 1999 to May 2000	0.8	4.4	0.3	4.3	−0.1	39.8	0.58	2422
Oct 2000 to May 2001	0.0	3.5	0.6	3.3	3.9	22.3	0.77	2855

[a]Here $m_{\Delta x,\Delta y}$ and $\sigma_{\Delta x,\Delta y}$ are mean and standard deviation, respectively, of the differences in the x and y directions; $m_{\Delta\theta}$ and $\sigma_{\Delta\theta}$ are mean and standard deviation, respectively, of the directional differences between the drift vectors; ρ^2 is squared correlation between the two drift vectors; and N is number of samples. Units are km d^{-1}.

Compared to the daily drift results, the squared correlation (ρ^2) between monthly model and RGPS drifts is quite different: on average ρ^2 has decreased for PIOMAS, increased for ECCO2, decreased for NPS, and decreased slightly for LANL. The ρ^2 of PIOMAS, ECCO2, and LANL are now more in the same range (0.4–0.6). Differences between ρ^2 in Tables 2 and 3 can be attributed to the following: (1) the daily drift comparisons are performed at available buoy locations, and buoys are deployed typically on older ice and away from thinner seasonal ice; and (2) the monthly comparisons using RGPS ice drift provide a more spatially extensive sampling of model-data differences. At the monthly timescale, the overall performance of the four models (except for the NPS simulations) seems to be more comparable than that suggested in Table 2.

[23] To explore whether the simulated drifts are superior away from the coast, we calculate the monthly model-RGPS differences for only drift tracks that are more than 400 km from the coast. When these results (Table 3) are contrasted with those obtained from the entire RGPS domain, it can be seen that there is a remarkable increase in the squared correlation between the monthly model and RGPS ice drift for all years. The $\sigma_{\Delta x,\Delta y}$ are also lower. The NPS results are an exception and are attributable to factors discussed in Section 2.1.3. Overall, the results suggest that coastal ice drifts are not simulated as well perhaps because of the treatment of the boundary conditions or deficiencies in the forcing or rheology used. Nevertheless, this behavior seems to be a common characteristic. Difficulties in simulating coastal motion are also manifest in the spatial field of differences between model and RGPS, as discussed below.

[24] Figure 2 depicts the spatial distribution of average monthly drift differences for the four winters over that part of the Arctic Ocean covered by RGPS observations. In the central Arctic Ocean, the average differences are within 1 km d^{-1} (light blue and yellow). Common among the results from the 4 years are the large negative differences (dark blue), of generally slower model drift (by more than 2 km d^{-1}), off the Alaskan and east Siberian coasts. The differences are most pronounced in the NPS model drift; as mentioned earlier, these results highlighted the overall effect of using simplified model thermodynamics and ice strength parameterization, which have been shown to result in overly low simulated ice drifts [*Maslowski and Lipscomb*, 2003]. Certainly, the thicker NPS ice cover (Figure 1) would have an additional effect on the overall drift speed because of attenuated response to wind forcing. Again, these discrepancies that are common to all the model simulations, are worth investigating to learn whether they are due to coastal

Table 3. Differences Between Monthly Model and RGPS Ice Drifts for the Entire RGPS Domain and for Only Regions That Are More Than 400 km From the Coast[a]

	$m_{\Delta x}$		$\sigma_{\Delta x}$		$m_{\Delta y}$		$\sigma_{\Delta y}$		$m_{\Delta\theta}$		$\sigma_{\Delta\theta}$		ρ^2		N	
	Entire RGPS Domain	Regions >400 km From Coast	Entire RGPS Domain	Regions >400 km From Coast	Entire RGPS Domain	Regions >400 km From Coast	Entire RGPS Domain	Regions >400 km From Coast	Entire RGPS Domain	Regions >400 km From Coast	Entire RGPS Domain	Regions >400 km From Coast	Entire RGPS Domain	Regions >400 km From Coast	Entire RGPS Domain	Regions >400 km From Coast
							PIOMAS									
Nov 1996 to Apr 1997	0.0	−0.1	1.2	0.7	1.1	0.0	1.1	0.6	7.4	8.0	48.1	38.2	0.47	0.67	36,640	20,635
Nov 1997 to Apr 1998	−0.5	−0.8	1.3	0.8	1.5	0.4	1.5	0.7	15.0	23.1	40.0	34.0	0.35	0.52	32,421	17,287
Nov 1998 to Apr 1999	0.2	0.0	1.1	0.7	1.0	−0.3	1.0	0.8	10.5	11.7	51.2	42.3	0.37	0.56	43,177	22,645
Nov 1999 to Apr 2000	0.3	0.3	1.0	0.6	1.1	0.1	1.1	0.6	16.2	24.2	53.8	40.1	0.37	0.54	41,950	22,093
Nov 2000 to Apr 2001	0.0	0.3	1.4	0.8	1.6	0.1	1.6	0.7	11.1	11.2	39.3	29.9	0.51	0.64	41,633	22,161
Nov 2004 to Apr 2005	0.3	0.3	1.3	1.0	1.3	0.1	1.3	0.8	12.4	14.5	41.8	25.5	0.57	0.68	36,901	20,873
							ECCO2									
Nov 1996 to Apr 1997	0.0	0.1	1.3	1.0	1.0	−0.4	1.0	0.7	−5.0	0.2	39.0	29.6	0.52	0.69	36,646	20,635
Nov 1997 to Apr 1998	0.1	0.0	1.4	0.8	1.4	0.2	1.4	0.8	−6.4	−6.9	44.3	42.6	0.47	0.66	32,434	17,287
Nov 1998 to Apr 1999	−0.2	−0.3	1.1	0.8	0.9	0.1	0.9	0.8	−0.5	−6.0	48.0	42.7	0.47	0.54	43,209	22,645
Nov 1999 to Apr 2000	−0.3	−0.3	1.2	0.9	1.4	−0.4	1.4	1.0	9.4	7.3	42.1	30.1	0.34	0.52	41,959	22,093
Nov 2000 to Apr 2001	0.0	0.0	1.5	1.2	1.8	0.2	1.8	1.0	1.8	−0.7	50.7	43.8	0.36	0.47	41,638	22,161
Nov 2004 to Apr 2005	0.0	−0.1	1.3	1.1	1.1	−0.7	1.1	1.0	5.6	3.4	38.0	27.6	0.66	0.78	36,922	20,873
							NPS									
Nov 1996 to Apr 1997	−0.4	−0.4	1.5	1.1	1.5	0.9	1.5	1.0	8.4	11.4	52.5	47.1	0.21	0.33	36,646	20,635
Nov 1997 to Apr 1998	−0.9	−1.2	1.6	1.0	1.9	−1.0	1.9	1.1	−18.1	−21.2	65.8	68.6	0.05	0.05	32,434	17,287
Nov 1998 to Apr 1999	0.3	0.3	1.5	1.1	1.3	−0.1	1.3	1.1	7.9	−5.8	75.1	71.8	0.02	0.00	43,209	22,645
Nov 1999 to Apr 2000	−0.1	0.1	1.3	1.0	1.4	0.3	1.4	1.0	18.9	22.3	51.1	45.2	0.17	0.15	41,959	22,093
Nov 2000 to Apr 2001	−0.5	0.0	1.5	1.3	1.6	0.5	1.6	1.3	13.3	11.9	53.1	50.3	0.17	0.15	33,489	22,161
							LANL									
Nov 1996 to Apr 1997	0.3	0.2	1.0	0.8	0.9	0.1	0.9	0.6	2.4	0.4	39.8	32.0	0.57	0.68	36,347	20,635
Nov 1997 to Apr 1998	−0.3	−0.5	1.2	0.8	1.3	0.2	1.3	0.7	0.8	3.1	42.4	39.9	0.48	0.64	32,261	17,287
Nov 1998 to Apr 1999	0.1	0.0	1.0	0.7	0.9	0.0	0.9	0.7	3.6	2.7	44.8	45.6	0.56	0.66	42,905	22,645
Nov 1999 to Apr 2000	0.0	0.2	1.0	0.8	1.1	0.0	1.1	0.9	8.5	7.8	36.5	31.2	0.49	0.57	41,902	22,093
Nov 2000 to Apr 2001	−0.2	0.1	1.3	1.0	1.5	0.4	1.5	0.9	1.7	−3.1	38.7	35.1	0.49	0.54	41,457	22,161

[a]Here $m_{\Delta x,\Delta y}$ and $\sigma_{\Delta x,\Delta y}$ are mean and standard deviation, respectively, of the differences in the x and y directions; $m_{\Delta\theta}$ and $\sigma_{\Delta\theta}$ are mean and standard deviation, respectively, of the directional differences between the drift vectors; ρ^2 is squared correlation between the two drift vectors; and N *is* number of samples. RRGPS, RADARSAT Geophysical Processor System. Units are km d^{-1}.

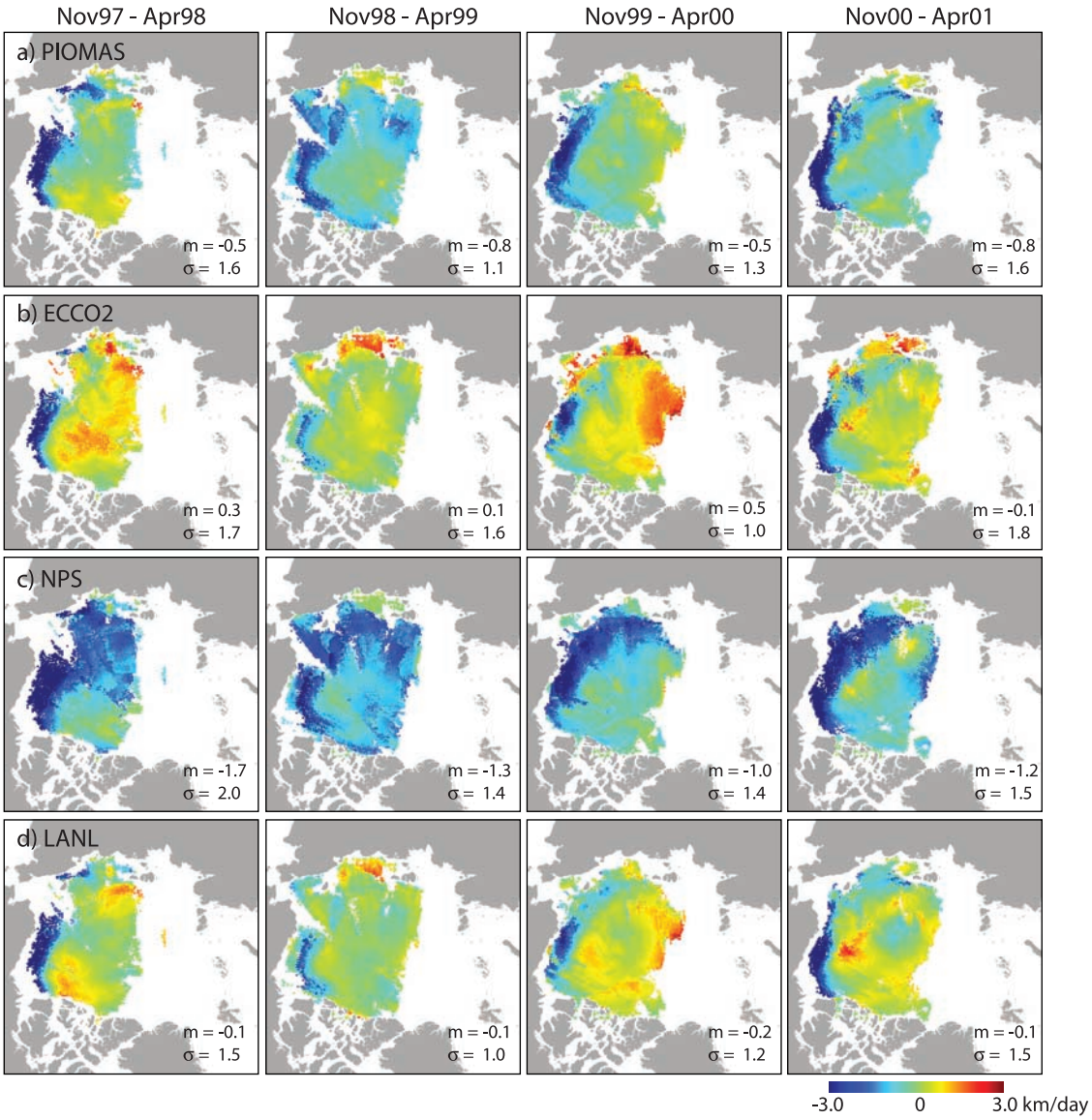

Figure 2. Differences between monthly model and RGPS displacements magnitudes for four winters (November–April). (a) PIOMAS, (b) ECCO2, (c) NPS, and (d) LANL (units: km d^{-1}).

wind forcing or model behavior and also whether other models exhibit the similar behavior.

3.4. Fram Strait Area Flux

[25] One metric that is widely used in model development, especially for tuning model parameters, is that of ice area outflow at the Fram Strait; this export of sea ice is of interest because of its importance in the mass balance of the Arctic ice cover and its potential impact on convective overturning in the Greenland Sea. In Figure 3, the simulated winter ice area outflow is compared to satellite observations [*Kwok and Rothrock*, 1999; *Kwok et al.*, 2004]. The interannual variability seems to be well simulated. However, the LANL outflow stands out as being higher by $\sim 400 \times 10^3$ km^2. This is contrary to the LANL-RGPS results (in Tables 2 and 3) obtained thus far, which showed no significant anomaly in the LANL ice drift in the western Arctic. Since RGPS observations do not extend to the eastern Arctic, we compare one winter's of ice drift from satellite passive microwave observations [*Kwok et al.*, 1998] with those of the LANL model. Indeed, the comparison shows that while the LANL ice drift seems to be reasonable (i.e., comparable to satellite ice drift) in other parts of the Arctic Ocean, the LANL ice drift is much higher (>2–3 km d^{-1}) in the Kara Sea, in the eastern Arctic over the Nansen Basin and in the Fram Strait. At the Fram Strait, this increased drift speed results in a higher area outflow for the years compared. The increased area outflow most likely is due to the surface forcing used (winds and ocean currents), but also could be attributable partly to the thickness of the LANL ice cover in this region (see Figure 1). Compared to the other model fields, there is a large expanse of sea ice that is much thinner (1–1.5 m thick) covering much of the Nansen Basin. This highlights the importance of a spatially extensive ice drift data set for

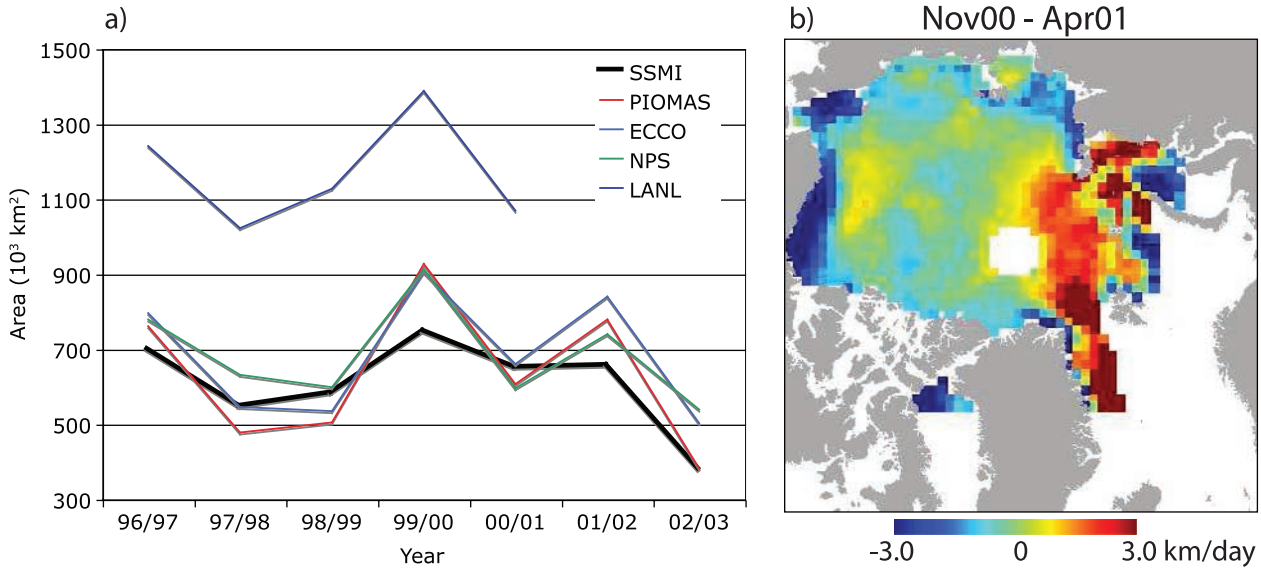

Figure 3. (a) Comparison of model Fram Strait sea ice outflow with satellite estimates and (b) spatial differences between LANL model and satellite ice drift (km d^{-1}) for one winter (November 2000 to April 2001).

capturing the pan-Arctic response of coupled ice-ocean models or the anomalies in the forcing data sets.

4. Regional Drift and Deformation

[26] Spatial gradients and ice drifts at seasonal and regional scales are examined in this section. Rather than short-term responses, the objective here is to capture the seasonal behavior at these longer length scales by comparison with RGPS ice drifts and gradients.

4.1. Seasonal Drift and Regional Deformation

[27] In this section, we partition the available winter RGPS coverage of the Arctic Ocean into five regions and examine the net seasonal advection and deformation of the boundaries of each individual region over the winter (Figure 4). Depending on the RGPS coverage of a particular year, the southern boundaries of the regions vary from year to year. Henceforth, we designate region i as S_i. For the years considered here, the sea ice cover of the Beaufort and Chukchi Seas, in S_1 and S_2, are predominantly seasonal and thus thinner. S_3 contains a mixture of ice types with seasonal ice in the south. The central Arctic and Canada Basin (within S_4 and S_5) are inside the perennial ice zone and generally have higher fractions of older and thicker ice. All regions, except for S_4, are subject to direct coastal influences from the perspective of ice mechanics and thermodynamics. In the fall, the southern ice edges of S_1, S_2 and S_3 are generally exposed to the open ocean.

[28] Figure 4 shows, for 5 years (1997 to 2001), the variability of the coverage and deformation of the five regions as manifested by the boundaries between November and the end of April. For each year, Figure 4 shows (1) the initial coverage and boundaries of the five regions at the beginning of November, (2) the advected and deformed regions at the end of April from RGPS ice drift (in color), and (3) the same regional boundaries at the end of April from model ice drift (in black). Vectors (model in black; RGPS in red) near the center of each region represent the average displacement of the region's boundaries. Drift tracks of boundary samples that define the regions are constructed as in the above section: starting from an initial location, gridded model motion fields are interpolated to propagate individual drift tracks on a daily basis.

[29] At the large scale, the mean advection of the regions and their defining boundaries are expressions of the large-scale circulation patterns. At the small scale, the response of the ice cover to large-scale gradients and coastal boundaries is concentrated along narrow zones of fractures and these give the boundaries the smaller-scale structures in Figure 4. Generally, all the models capture the large-scale wind-driven anticyclonic motion during the winter quite well. In detail, however, variability in model behavior is high. Boundaries from model drift could lead or lag the RGPS boundaries. Occasionally, the curvature of the boundaries could be reversed. Here, we select two broad measures of the correspondence between model and data: the total displacement of individual regions computed as the average of the displacements of the boundary points (Table 4), and the regional area change (or divergence) between November and April (Table 5).

[30] Table 4 shows the seasonal displacement of each region as a fraction of the RGPS displacement and the directional difference between the displacement vectors. S_1, during the winter of 1998, saw the largest average displacement of 555 km, while the 93 km displacement of S_4 in 1999 was the smallest exhibited. The model-derived displacement ranges between 0.2 and 2.4 times that of the RGPS displacements. Directional differences between the displacement vectors could be up to 110°. The last two rows of Table 4 show the mean and standard deviation for each parameter over the 5 years and five regions. On average, the NPS ice drift stand out as giving regional displacements that are consistently lower (mean $D_{model}/D_{RGPS} = 0.5$) than those

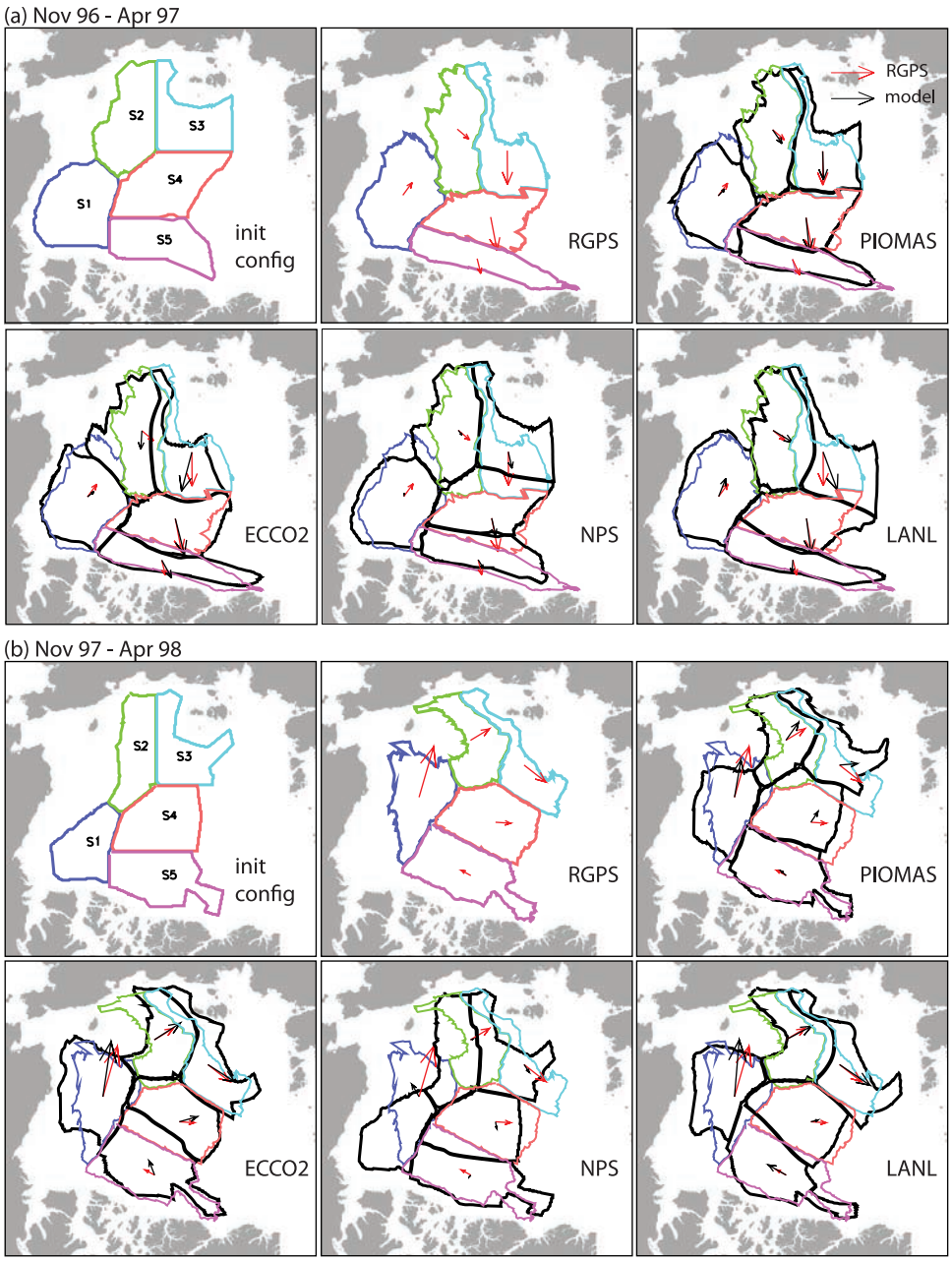

Figure 4. Differences in regional advection and deformation between model and RGPS estimates. (a) November 1996 to April 1997, (b) November 1997 to April 1998, (c) November 1998 to April 1999, (d) November 1999 to April 2000, and (e) November 2000 to April 2001. Model-derived regional boundaries are in black, while those from the RGPS are in color. Vectors (model is in black, and RGPS is in red) near the center of each region show the average displacement of the boundary samples computed from model and RGPS data.

of the RGPS. This is also evident in the generally lower NPS ice drift seen in Figure 2.

[31] The percentage regional area change between November and April (or equivalently, divergence) and the difference between model and RGPS percentages are shown in Table 5. The RGPS data shows that the regional divergence ranges between −14% and 37% over the 6 winter months. Except for the first year, divergence in S_1 is higher than in all other regions for all the years. Extremes in the differences between model and RGPS area change data can be up to 31% too high or 23% too low. Also shown (the last five rows) are the averages for each region for the 5 years. Since the divergence signal is so large in S_1, on average the differences are smaller than the signal. For regions with very small net area changes, the differences can be as large as the actual RGPS-derived divergence. As can be seen in the variability of this measure, net divergence is one of the more difficult parameters to model because it is dependent on accurate simulation of very small velocity gradients or strain rates. Comparisons of the model-RGPS regional advection

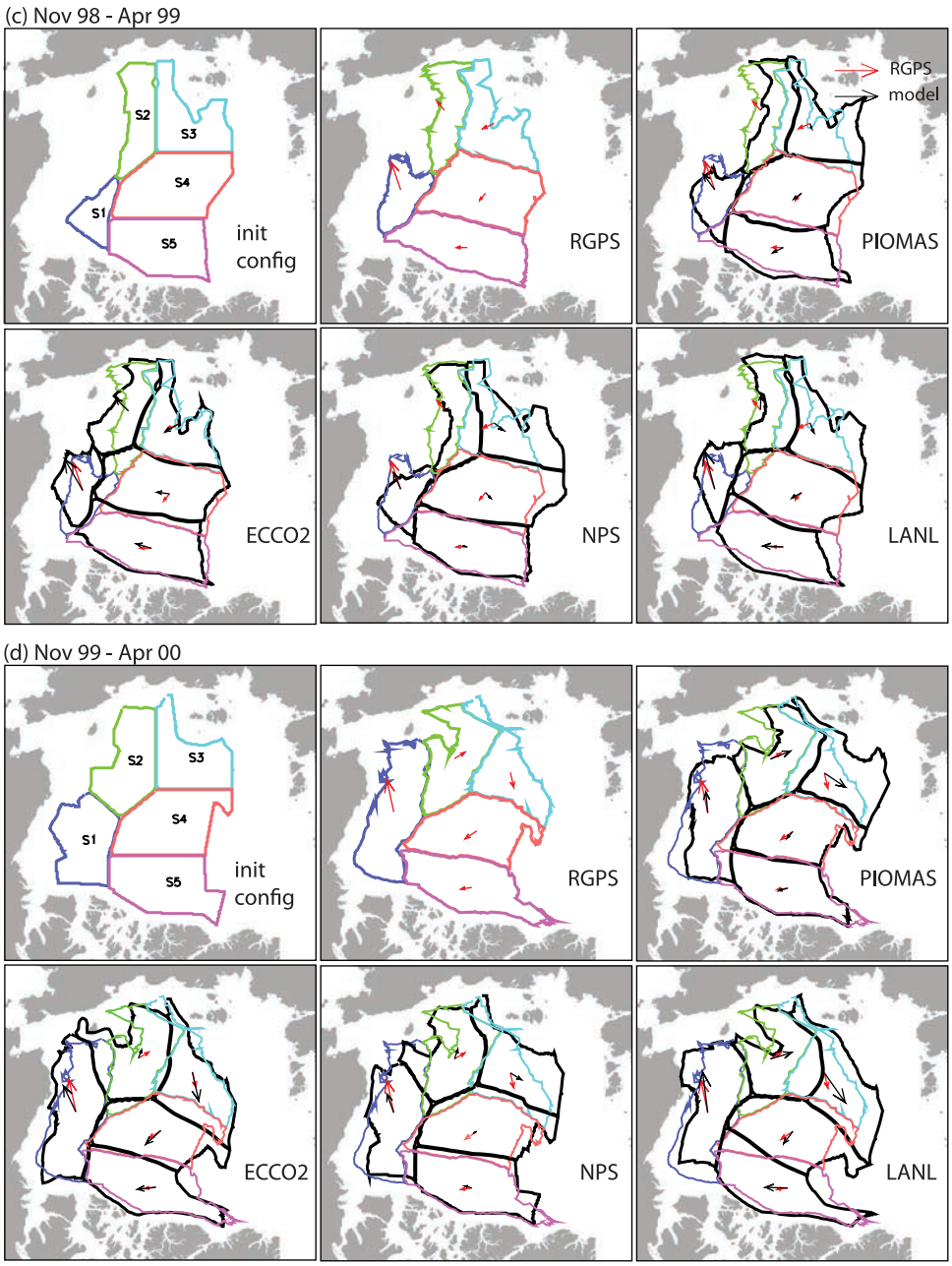

Figure 4. (continued)

and deformation at the seasonal timescale shown here capture the longer timescale integrated behavior of individual models that is not available from just first-order drift differences (like those in Tables 1 and 2).

4.2. Correlation of Regional Deformation Time Series

[32] The previous subsection explored the overall seasonal drift and divergence of five regions. At a shorter timescale, we can examine the temporal correlations of the time series of 6-day deformation of these five regions from model and RGPS ice motion. The regional deformation defined by divergence, vorticity, and shear is computed as in equation (1). In this case, u_x, u_y, v_x, v_y are the spatial gradients in ice motion computed using a line integral around the boundary of each region. The line segments connecting the boundary define the path of the integral. Interpretively, $\nabla \cdot u$ is a measure of the rate of area change, ζ is the principal measure of rotation rate, and e is the scalar magnitude of shear. Figure 5 shows one example of the time series of 6-day regional shear derived from ice drift from the four models and the RGPS. The particular region in this example is S_1 for the time period between November 2000 and April 2001. Relative correlations between the model and RGPS time series can be seen in this example.

[33] Table 6 summarizes the squared correlations between the model and RGPS time series of 6-day divergence, vorticity, and shear for the five winter seasons. Again, the variability in performance is high with the models accounting from 0 to 24% of the variance in the time series of divergence, 0 to 76% of the vorticity, and 0 to 69% of shear.

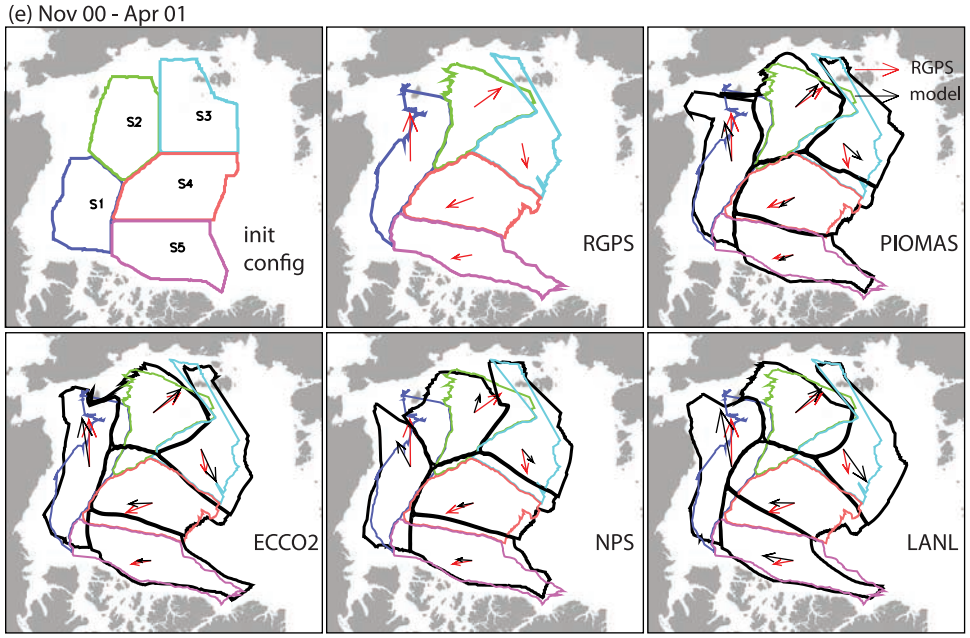

Figure 4. (continued)

Table 4. Average of the Displacements (D) of the Boundary Points of the Five Regions Between November and April, the Model Displacements as a Fraction of the RGPS Displacements, and the Directional Differences ($\Delta\theta$) Between the Model and RGPS Displacement Vectors[a]

Region	D_{RGPS} (km) (RGPS)	D_{model}/D_{RGPS} PIOMAS	ECCO2	NPS	LANL	$\Delta\theta$ (deg) PIOMAS	ECCO2	NPS	LANL
				Nov 1996 to Apr 1997					
S_1	166	0.6	0.5	0.2	1.2	−6.8	−14.7	28.2	14.7
S_2	162	1.1	1.2	0.4	1.5	−15.3	−53.3	−11.0	9.1
S_3	358	0.8	1.2	0.5	1.2	1.4	−15.3	12.4	20.1
S_4	362	1.0	1.1	0.5	1.0	−5.1	3.6	1.8	−3.4
S_5	163	1.1	1.3	0.6	0.9	11.2	15.4	18.3	−18.4
				Nov 1997 to Apr 1998					
S_1	555	0.7	1.1	0.3	1.1	6.3	7.6	46.1	11.3
S_2	233	1.0	1.4	0.1	1.3	23.7	1.6	−16.5	−3.2
S_3	290	0.6	1.2	0.3	1.3	42.6	5.5	−18.2	4.0
S_4	160	0.8	1.2	0.4	0.5	59.8	19.4	−76.1	17.4
S_5	113	0.7	1.4	0.2	1.9	−12.6	−39.9	79.4	−1.0
				Nov 1998 to Apr 1999					
S_1	307	0.6	1.2	0.6	1.4	16.9	11.0	4.5	−4.3
S_2	117	0.5	1.6	0.3	1.3	−76.8	5.7	−109.9	−42.3
S_3	128	0.4	1.2	0.9	0.8	83.6	6.2	111.4	87.3
S_4	93	1.1	1.4	0.9	1.2	−12.9	−57.3	82.5	−20.7
S_5	111	1.1	1.5	0.4	1.9	26.0	−16.0	−14.6	−2.8
				Nov 1999 to Apr 2000					
S_1	344	0.6	0.9	0.6	1.3	−6.4	13.6	8.2	−4.6
S_2	124	1.8	0.7	0.9	1.9	−8.6	38.9	40.3	−13.7
S_3	160	1.7	1.9	0.8	2.4	43.3	−0.5	45.2	22.3
S_4	146	0.6	1.5	0.2	1.1	15.4	8.1	−5.2	19.3
S_5	112	0.9	1.7	0.7	2.1	8.4	−1.3	−24.0	−9.6
				Nov 2000 to Apr 2001					
S_1	489	0.8	1.0	0.6	1.2	9.7	7.9	27.6	10.3
S_2	334	1.0	1.1	0.6	1.1	9.1	5.2	36.8	7.2
S_3	247	1.0	1.5	0.7	1.7	36.6	13.5	28.9	24.1
S_4	287	0.6	0.8	0.6	0.9	11.8	−18.3	−8.7	−20.8
S_5	201	0.7	0.7	0.8	1.5	10.6	−9.0	−14.0	−19.2
Mean		0.9	1.2	0.5	1.3	10.9	−2.5	10.9	3.3
SD		0.3	0.3	0.2	0.4	30.1	22.0	46.7	24.0

[a]Negative to the right of the RGPS vector.

Table 5. Percentage Area Changes ($\Delta A/A \times 100$) of the Five Regions Between November and April and Their Percentage Differences From the RGPS Estimates

	$\Delta A/A \times 100$					$((\Delta A/A)_{\text{model}} - (\Delta A/A)_R) \times 100$			
Region	RGPS	PIOMAS	ECCO2	NPS	LANL	PIOMAS-RGPS	ECCO2- RGPS	NPS-RGPS	LANL-RGPS
					Nov 1996 to Apr 1997				
S_1	10.2	3.2	6.3	5.2	14.6	−7.0	−3.9	−5.0	4.4
S_2	0.5	12.8	7.7	10.1	14.8	12.3	7.2	9.6	14.3
S_3	−0.8	9.2	−1.8	11.5	12.6	10.0	−1.0	12.3	13.4
S_4	−13.4	−10.8	−7.4	4.4	−1.3	2.6	6.0	17.8	12.1
S_5	−8.5	−24.9	−21.1	−4.9	−9.4	−16.4	−12.6	3.6	−0.9
					Nov 1997 to Apr 1998				
S_1	33.2	24.2	57.9	11.2	32.4	−9.0	24.7	−22.0	−0.8
S_2	−1.7	−3.9	3.4	7.7	14.0	−2.2	5.1	9.4	15.7
S_3	−8.0	1.3	9.6	11.9	16.4	9.3	17.6	19.9	24.4
S_4	8.8	9.0	−9.9	10.2	9.9	0.2	−18.7	1.4	1.1
S_5	17.8	16.7	30.4	7.7	16.6	−1.1	12.6	−10.1	−1.2
					Nov 1998 to Apr 1999				
S_1	36.6	20.5	36.3	13.5	28.1	−16.1	−0.3	−23.1	−8.5
S_2	−3.4	0.6	2.0	6.0	8.6	4.0	5.4	9.4	12.0
S_3	0.5	0.3	4.7	10.2	13.2	−0.2	4.2	9.7	12.7
S_4	1.0	8.4	3.7	11.8	13.0	7.4	2.7	10.8	12.0
S_5	16.5	0.8	28.2	12.9	11.7	−15.7	11.7	−3.6	−4.8
					Nov 1999 to Apr 2000				
S_1	37.9	26.7	28.8	18.8	23.7	−11.2	−9.1	−19.1	−14.2
S_2	0.1	6.6	18.6	5.5	10.8	6.5	18.5	5.4	10.7
S_3	−6.8	15.6	20.7	13.5	24.2	22.4	27.5	20.3	31.0
S_4	−0.2	5.4	−2.9	11.8	7.6	5.6	−2.7	12.0	7.8
S_5	1.6	−10.4	−2.9	6.5	4.5	−12.0	−4.5	4.9	2.9
					Nov 2000 to Apr 2001				
S_1	12.8	38.8	29.6	17.7	25.7	26.0	16.8	4.9	12.9
S_2	−6.2	10.9	6.9	5.8	11.7	17.1	13.1	12.0	17.9
S_3	−14.4	0.8	6.9	16.3	12.2	15.2	21.3	30.7	26.6
S_4	3.0	17.1	3.8	14.6	16.6	14.1	0.8	11.6	13.6
S_5	−1.0	−6.5	12.3	5.4	14.0	−5.5	13.3	6.4	15.0
					Average				
S_1	26.1	22.7	31.8	13.3	24.9	−3.5	5.6	−12.9	−1.2
S_2	−2.1	5.4	7.7	7.0	12.0	7.5	9.9	9.2	14.1
S_3	−5.9	5.4	8.0	12.7	15.7	11.3	13.9	18.6	21.6
S_4	−0.2	5.8	−2.5	10.6	9.2	6.0	−2.4	10.7	9.3
S_5	5.3	−4.9	9.4	5.5	7.5	−10.1	4.1	0.2	2.2

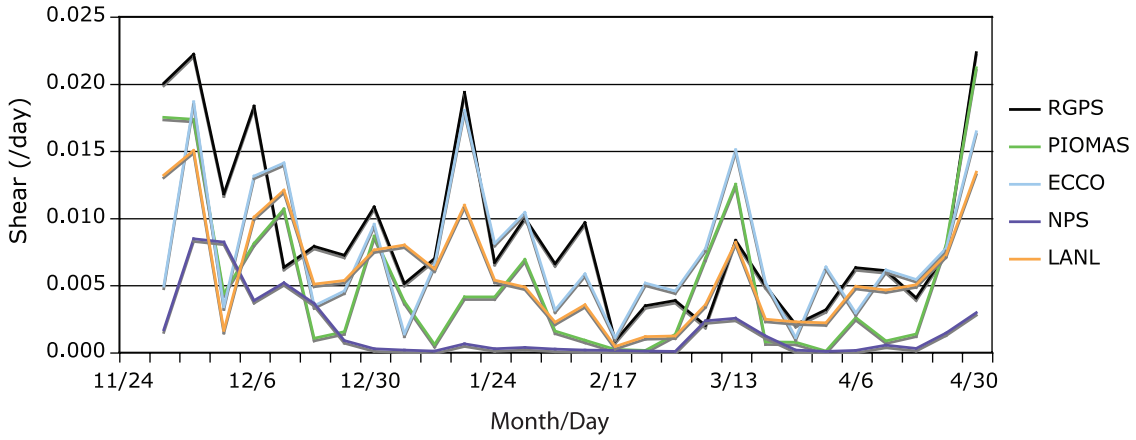

Figure 5. One example of the time series of 6-day regional shear derived from model and RGPS ice drift. The particular region in this example is S_1 for the time period between November 2000 and April 2001. Squared correlation between the time series of 6-day divergence, vorticity, and shear from the model simulations and RGPS observations for the five regions are shown in Table 6.

Table 6. Squared Correlation (×100) Between the Time Series of 6-day Divergence, Vorticity, and Shear From the Model Simulations and RGPS Observations for the Five Regions

	Divergence				Vorticity				Shear			
Region	PIOMAS	ECCO2	NPS	LANL	PIOMAS	ECCO2	NPS	LANL	PIOMAS	ECCO2	NPS	LANL
					Nov 1996 to Apr 1997							
S_1	0	11	0	0	48	58	3	76	13	12	3	16
S_2	6	15	7	16	6	15	7	16	56	47	25	64
S_3	0	4	5	9	27	36	10	32	27	44	26	32
S_4	12	18	0	20	36	57	1	25	7	48	24	36
S_5	58	73	42	60	57	65	12	66	66	63	45	60
					Nov 1997 to Apr 1998							
S_1	30	24	15	27	30	24	15	27	44	43	3	45
S_2	18	13	0	21	18	13	0	21	29	32	30	50
S_3	0	0	1	0	0	0	1	0	21	20	31	30
S_4	1	6	2	0	1	6	2	0	9	11	0	22
S_5	29	18	7	29	29	18	7	29	6	12	3	20
					Nov 1998 to Apr 1999							
S_1	10	13	16	12	34	45	19	29	47	46	4	51
S_2	27	29	11	6	27	29	11	6	6	33	8	15
S_3	7	8	1	5	50	56	12	55	35	46	3	42
S_4	6	0	1	0	42	68	24	66	9	29	1	14
S_5	9	11	9	14	0	39	12	35	37	53	9	42
					Nov 1999 to Apr 2000							
S_1	4	10	1	7	27	19	37	28	3	7	9	10
S_2	1	0	0	0	1	0	0	0	4	18	3	23
S_3	0	2	0	0	11	27	2	16	0	0	10	0
S_4	0	2	0	0	31	52	11	42	0	4	1	1
S_5	0	7	0	1	23	31	16	19	6	8	24	3
					Nov 2000 to Apr 2001							
S_1	8	18	23	34	67	50	35	76	60	42	26	48
S_2	6	13	4	8	6	13	4	8	69	19	3	35
S_3	6	13	0	8	60	70	56	60	29	44	36	30
S_4	0	0	0	3	72	77	16	67	14	23	5	8
S_5	10	13	3	5	37	69	27	54	4	9	29	15
					Average							
S_1	10	15	11	16	46	45	27	54	33	30	9	34
S_2	12	14	5	10	12	14	5	10	33	30	14	38
S_3	3	6	1	4	34	44	16	40	23	31	21	27
S_4	4	5	1	5	44	61	13	49	8	23	6	16
S_5	21	24	12	22	28	52	16	44	24	29	22	28

On average, the models are best at simulating the time series of regional vorticity, followed by shear and divergence. The simulation of divergence is remarkably poor. Of note is that the squared correlations of time series of regional deformations are uniformly poor in all the models between November 1999 and April 2000. Interestingly, this one winter does not stand out as clearly in the earlier comparisons (Tables 1, 2, 3, 4, and 5). The quality of the 6-day vorticity and shear time series seems much better simulated in the preceding years and in the following year. These 5 years of results seem to indicate significant interannual variability in the quality of simulated regional deformation.

4.3. Net Winter Deformation at ~10 km Length Scale

[34] Figure 6 contrasts the net seasonal deformation (divergence, vorticity, and shear) of one winter (November 1997 to April 1998) at the length scale of the RGPS Lagrangian cells (~10 km). This examination provides another temporally integrated measure of the performance of the models but at a higher resolution. Similar to the approaches above, model drift tracks for the entire season with an initial spacing of 10 km are constructed and the net deformation is computed at the end of April. The deformation at each Lagrangian cell is computed by first summing the velocity gradients over the period and then calculating the net divergence, vorticity, and shear as in equation (1).

[35] Figure 6 shows that there is a wealth of spatial details in the high-resolution RGPS depiction of the behavior of the ice cover at and near the length scale of the Lagrangian cells (~10 km). It is certainly not expected that current models should be able to reproduce these spatial details but it is interesting to note the similarities in the large-scale spatial patterns. The model results, except those from the NPS, seem to be able to reproduce the large-scale clockwise rotation (positive vorticity: light bluish pattern) of the central Arctic Ocean. The region of more intense rotation (deeper blue) just north of the Alaskan coast is missing in all the model results. It is also interesting to note that the counterclockwise rotation of the Lagrangian cells just north of the Anjou Islands and in the East Siberian Sea can be seen in all the simulations. In terms of divergence, the positive divergence zones (red) are concentrated near the

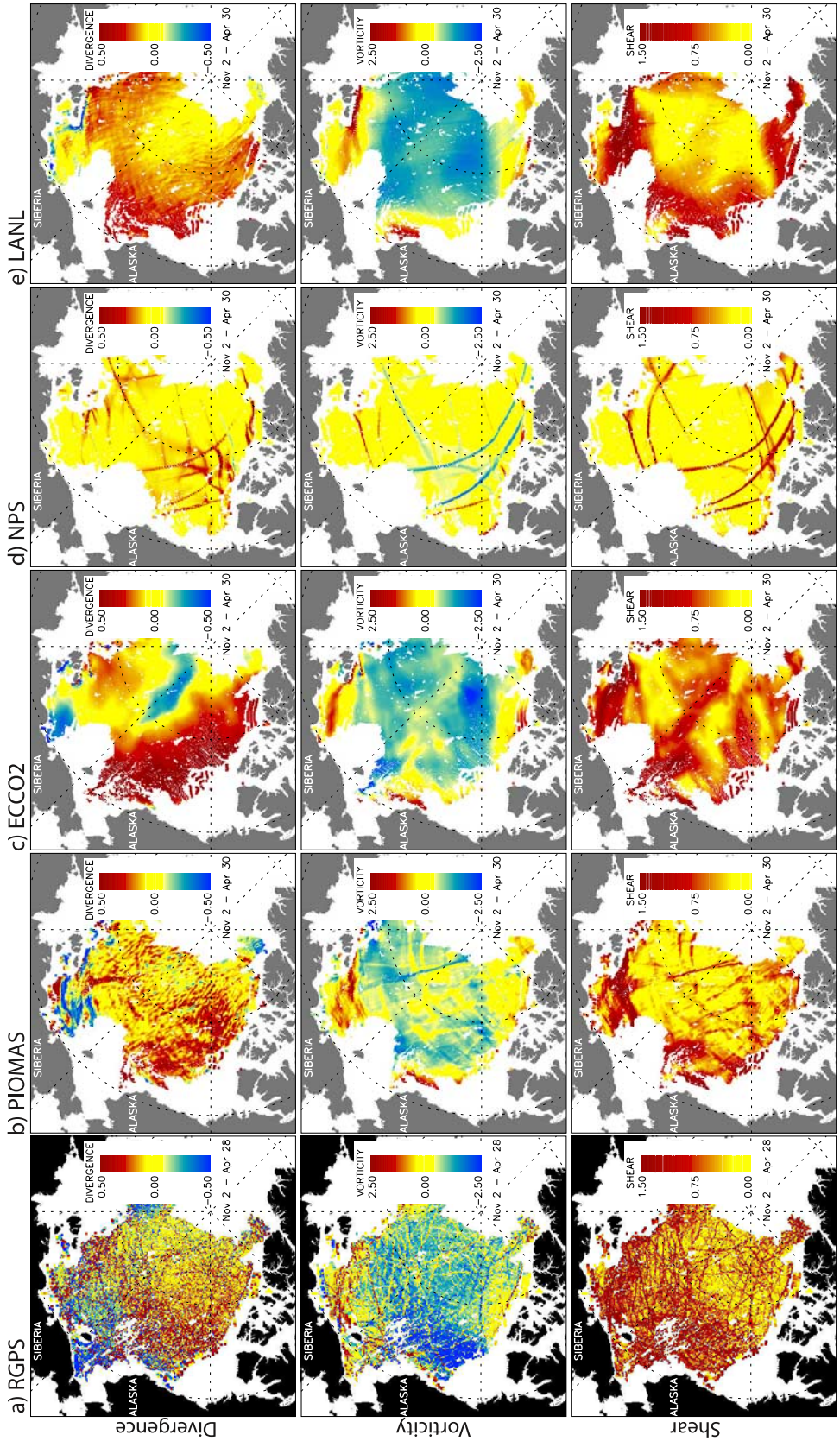

Figure 6. Contrast between the net winter deformation (divergence, vorticity, and shear) from model simulations and RGPS ice drift. (a) NPS, (b) PIOMAS, (c) ECCO2, (d) NPS, and (e) LANL (strain rate units: d^{-1}).

southern part, the margins, of the Arctic ice cover; convergence zones (blue) stand out in the E. Siberian Sea. The central part of the Arctic near the pole is somewhat more quiescent. Broadly, there seems to be some resemblance between the model fields and RGPS results. The NPS results are quite different in that these general patterns of divergence and vorticity are not produced; potentially, this could be due to the relatively thicker NPS ice cover (Figure 1) and thus higher ice strength and less responsive to external forcing. The map of net winter shear from the RGPS shows linear features that crisscross the Arctic Ocean at different orientations with an area of relative quiescence again near the pole. Visually, however, it is more difficult to locate any spatial correspondence in the shear patterns in the model and RGPS fields. The density of the RGPS linear patterns is significantly higher than that seen in the model maps. Perhaps this contrast between model and data could be exploited in future model improvements. An interesting question is whether increased model resolution would eventually produce similar details.

5. Deformation-Related Ice Production

[36] The seasonal ice volume produced in openings or fractures in the ice cover is examined here. In the RGPS, this volume production is estimated using the record of area changes of the Lagrangian cells and a simple ice growth model. We use the same procedures to compute the volume production using model ice drift. The intent here is not to evaluate the absolute ice production but to contrast the relative variability of the deformation-related area/ice production calculated from model and from high-resolution RGPS ice drift. Indeed, since we use an identical ice growth, the differences due to model thermodynamics are removed from this assessment. In this section, we first provide a brief review of the approach detailed by *Kwok et al.* [1995] and *Kwok and Cunningham* [2002]. Then, we discuss the regional ice production and contrast the differences in seasonal ice produced in the models and the RGPS.

5.1. Estimation of Ice Production in RGPS

[37] It is important to note that the thickness distributions in the RGPS products are of only seasonal ice created in openings of the ice cover from an initial time (usually November). Basal ice growth on existing sea ice is not included. The thickness distribution prior to the first observation is not known. Procedurally, increases/decreases in the area of a Lagrangian cell are interpreted as openings/closings of the ice cover. New ice is assumed to grow in openings; sea ice is ridged or rafted when the ice cover closes. Thus, only the ice volume and thickness due to seasonal ice growth in these openings and closings are estimated. The seasonal ice thickness distributions, $g_s(h)$, are from the cell area changes from ice drift, an ice growth model, and an assumed mechanical redistributor of sea ice. The ice growth rate is approximated as a function of the number of freezing degree days experienced by each age category using Lebedev's parameterization [*Maykut*, 1986] where $h = 1.33\ F^{0.58}$; h is ice thickness (cm) and F is the accumulated freezing degree days (K) derived from the IABP/POLES 2-m air temperature. The thickness redistributor uses a combination of rafting and pressure ridging to account for decreases in cell area. Ice less than 40 cm thick is rafted instead of ridged. Rafted ice is twice its original thickness and occupies half the area; ridged ice is five times its original thickness [*Parmerter and Coon*, 1972] and occupies a quarter of the area. At each time step, the thickness distribution within a cell is updated. In the RGPS products, the seasonal thickness distributions of undeformed ice in the openings and ridged/rafted ice are kept track of separately. Uncertainties in ice production associated with noise in the RGPS ice drift is discussed by *Kwok and Cunningham* [2002].

5.2. Model and RGPS Ice Production

[38] Four years of deformation-related ice production (within the RGPS domains shown in Figure 4) from the models and the RGPS are shown in Figure 7. Model ice production is computed in the same manner as that of the RGPS procedures except that RGPS data is substituted with model kinematics. As above, drift tracks with the same temporal samplings are constructed from model motion fields. The results are not unexpected: the RGPS winter ice production is higher than the models for all 4 years because of the ice production associated with small-scale kinematics (length scale $\sim$5–10 km). It is also expected that models with larger grid spacing (e.g., LANL) would tend to underestimate ice production more than models with finer grid spacing because area changes associated with smaller-scale openings and closings are not resolved in coarser models. In fact, the LANL ice production is only somewhat lower than the other models. Since net grid area changes represent the net of openings and closings, we expected small-scale changes associated with those two processes are under-represented or not resolved as grid spacing increases. The NPS results again highlight the possible effect of lower sea ice drift and variability associated with using simplified model thermodynamics and ice strength parameterizations [*Maslowski and Lipscomb*, 2003].

[39] During the winter of November 1997 through April 1998, the NPS simulations produced only half of the RGPS ice volume. The model results, however, are not consistent relative to each other in terms of ice production, i.e., they do not rank in the same order from year to year. Also, the spread in the ice production is fairly wide. In the winter of November 1997 through April 1998, the difference between the model with lowest and highest ice production is almost 300 km^3. The spread in ice production is much narrower during the last year. Small differences between model and data measured at shorter time and spatial scales may be amplified and propagate in time and space, and thus affect long-range climate simulations.

6. Cracks and Fractures

[40] It is also not clear how well the models here can resolve small-scale kinematics that are associated with cracks and fractures. Deformation-related ice production is dependent on small-scale variability of ice drift (the response of the ice cover to large-scale gradients in atmospheric and ocean forcing is concentrated in subgrid-scale fractures and cracks). Cracks and fractures in the ice cover are an expression of the mechanical response of the sea ice to atmospheric and ocean forcings. As the grid spacing of

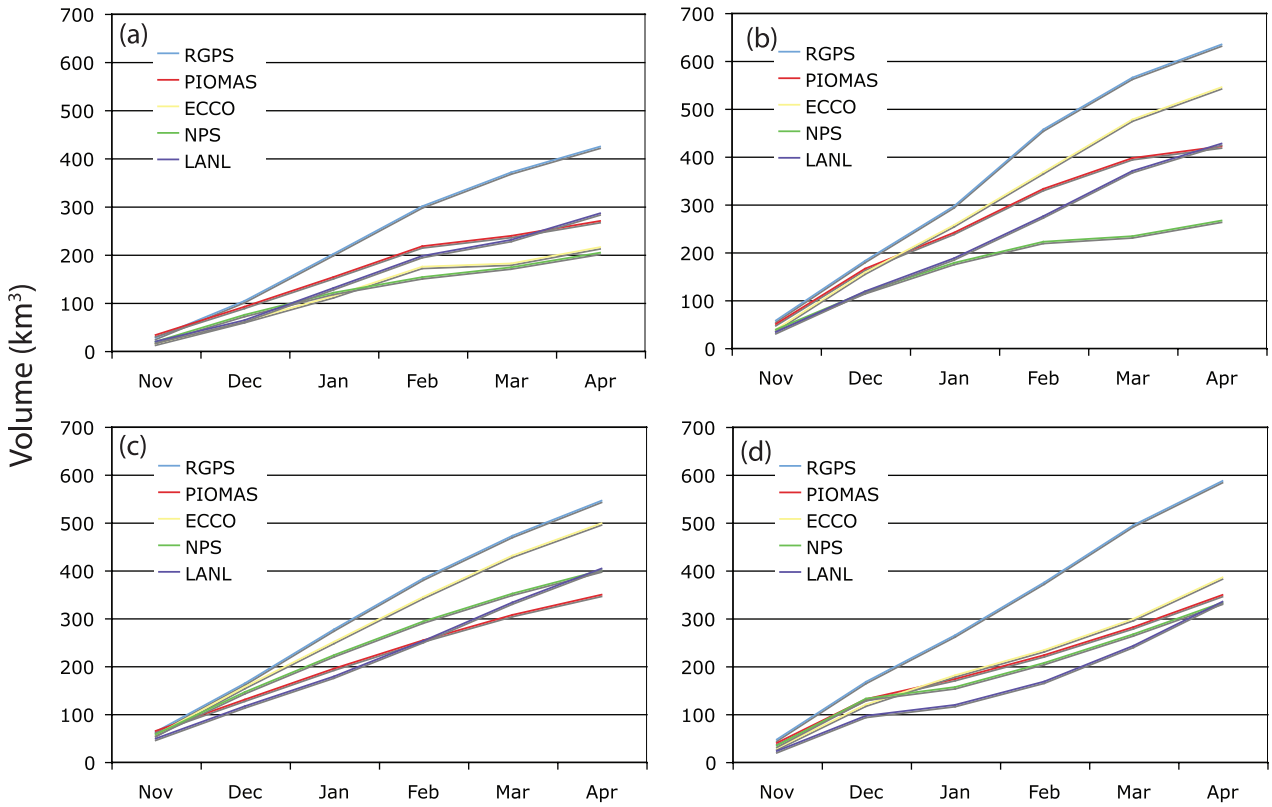

Figure 7. Deformation-related volume production. (a) November 1996 to April 1997, (b) November 1997 to April 1998, (c) November 1998 to April 1999, and (d) November 1999 to April 2000 (units: km^3).

sea ice models become finer, the question as to whether higher-resolution models are capable of capturing some of these cracks/fractures (or more appropriately linear kinematic features (LKFs)) seen in the RGPS deformation fields has been posed. Indeed, on the basis of simulations from a sea ice model similar to the LANL but configured at 9 km, *Maslowski and Lipscomb* [2003] report that the model with finer grid spacing produces long, narrow features in divergence and shear fields that resemble those observed in RGPS products. However, they stopped short of comparing their simulations with actual RGPS observations. *Hutchings et al.* [2005] demonstrate that these LKFs may be modeled with a viscous-plastic sea ice model, using an isotropic rheology: if the ice is assumed to be heterogeneous at the grid scale, and allowed to weaken in time, intersecting failure zones propagate across the region. To quantify such correspondence between model and RGPS data at these spatial scales is quite challenging because objective metrics are more difficult to devise. Simple spatial correlations of the LKFs require the models to reproduce the linear features in their correct locations (a tall order and perhaps not necessary especially when such spatial correspondence between fractures may not be the most important issue in climate simulations). In fact, their density and orientation pattern may be more important. A more in-depth discussion of this topic is, however, quite beyond the scope of this work.

[41] The intent of this section is to answer the above question at a very cursory level by visually inspecting the model and RGPS fields to identify correspondence between pairs of deformation fields. On the basis of all the fields from the 4 years that we examined, we found only half a dozen or so fields where there was some correspondence between model and data. It should be emphasized that only occasionally do we find what seem to be similar patterns of LKFs. Two of the best examples are shown in Figure 8. Certainly, the model shear fields do not show the richness in detail seen in the RGPS data. In the first example, the fracture patterns (indicated by arrows) in the Canada Basin seem to line up with the patterns seen in the RGPS. The LANL shear fields are more smeared because of the larger grid spacing/lower spatial resolution of that model. The second example shows a few fairly long LKFs that span a large fraction of the Arctic Ocean. The narrow feature in the middle of the Arctic Ocean is not visible in the LANL fields. We did not attempt at this time to document the likely conditions that are conducive to these occurrences. Needless to say, these are important issues to consider in the development and improvement of future ice models for the simulations of subgrid-scale processes at high resolution.

7. Conclusions

[42] The present examination of the utility of the RADARSAT Geophysical Processor System (RGPS) data for assessment of sea ice simulations is by no means exhaustive. We have illustrated several approaches for investigating model-data differences afforded by the RGPS

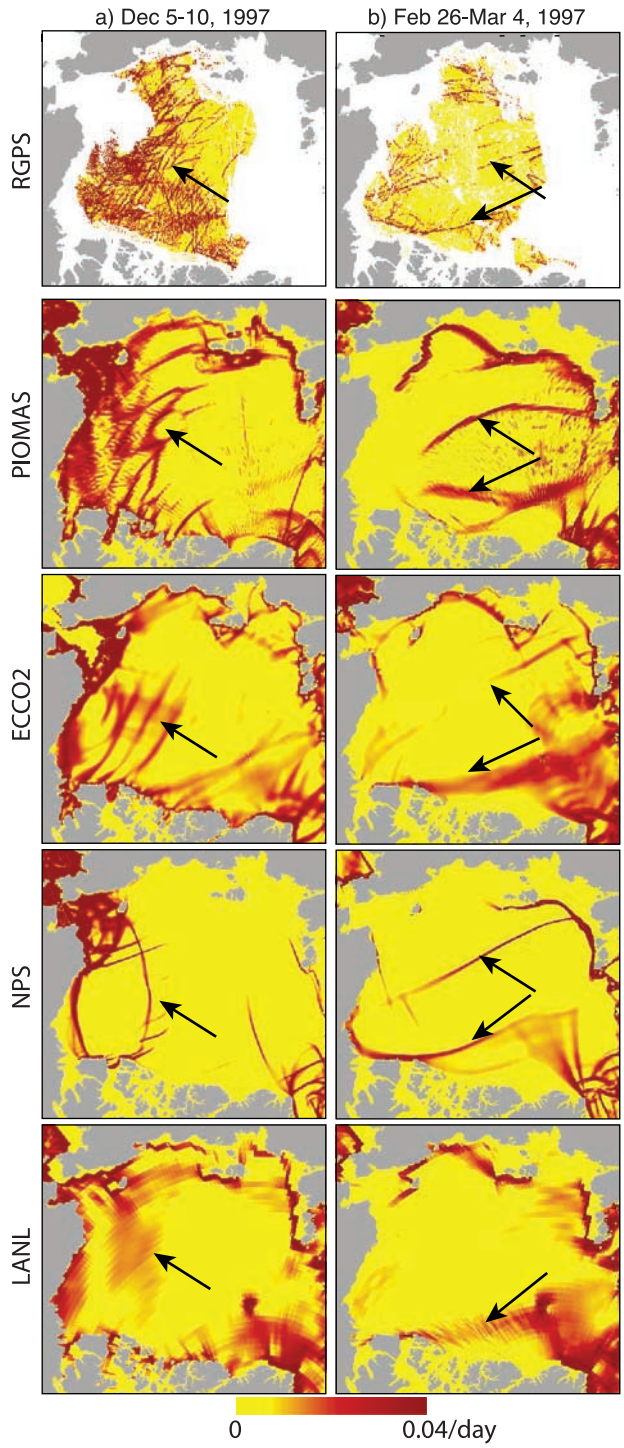

Figure 8. Two examples showing correspondence between patterns of 6-day shear deformation from model fields and the linear kinematic features from RGPS observations. (a) 5 December to 11 December 1997 and (b) 28 February to 4 March 1997. Fracture patterns (indicated by arrows) in the Canada Basin seem to line up with the patterns seen in the RGPS.

kinematics derived from high-resolution satellite radar data. Certainly, this is a first step (we have not explored all the objective measures that could be devised for assessing model simulations). The strengths of fine-scale RGPS sea ice kinematics are that they offer a level of spatial and temporal details that allow for closer examination of small-scale deformation at a near basin-scale context and at seasonal timescales. Gradients of ice drift at length scales of 10 km are available from specially deployed buoy arrays, but only with limited coverage in space and time.

[43] Daily sea ice drift from four models (the University of Washington (PIOMAS); Jet Propulsion Laboratory (ECCO2); Naval Postgraduate School (NPS); and, Los Alamos National Laboratory (LANL) - are used in our analysis). With four winters of RGPS data (1997 through 2001), we have been able to examine the (1) model ice drift from daily to seasonal timescales, (2) model ice drift and deformation at regional length and seasonal timescales, (3) impact of small-scale ice drift variability on deformation-related ice production, and (4) spatial distribution of deformation patterns in model fields. At seasonal timescales, model-RGPS comparisons allow us to investigate the integrated longer-term responses of the models to prescribed forcings in contrast to the short-term responses that one obtains from comparison with daily buoy drifts. The four models have different attributes; the assessment approaches show their behavior to be highly variable when compared to RGPS observations.

[44] In the above assessment, the large-scale circulation pattern of sea ice in the Arctic Ocean seems well simulated although there are distinct spatial structures indicating ice drift differences in the model-RGPS comparisons. These spatial structures are not evident in model-buoy comparisons because of the inadequate spatial sampling of the Arctic Ocean by drifting buoys. When compared with RGPS data, the common characteristics shared by the four models can be highlighted: (1) the ice drift along coastal Alaska is generally slower, (2) the skill in reproducing the time series of regional divergence of the ice cover is poor, and (3) the deformation-related volume production is consistently lower. Details of the differences within individual models and the RGPS data have not been fully explored. An in-depth analysis of the model differences is outside the scope of the present work. The approaches we have described provide a framework that enables better understanding of model behavior and perhaps will allow us to disentangle the differences due to model parameterization and atmospheric forcing.

[45] Of particular geophysical interest is the ability of models with finer grid spacing to reproduce fracture patterns found in RGPS data. Fractures and cracks are characteristics seen throughout the sea ice cover. Whether current models of sea ice mechanics are adequate for producing such structures remains a question. *Coon et al.* [2007], upon reviewing available deformation and stress data, suggest that a model including deformation at discontinuities and an anisotropic failure surface would better describe the observed behavior of pack ice at shorter length scales. Another relevant question is how well should these patterns be produced for improved climate simulations. Here, we only show that occasionally (and not very often) can we find in the model deformation fields patterns that seem to resemble

the linear features seen in RGPS. Future investigations will be able to take advantage of the RGPS observations for the assessment and the improvement of sea ice simulations.

Appendix A: Evaluation of Line Integrals Around a Polygon

[46] The line integral in equation (2):

$$u_x = \frac{1}{A} \oint u dy$$

is approximated by,

$$u_x = \frac{1}{A} \sum_{i=1}^{N} \frac{1}{2} (u_{i+1} + u_i)(y_{i+1} - y_i)$$

where N is the number of vertices that defines the region. The subscripts are cyclical (e.g., $u_{N+i} = u_i$). This results from the trapezoid integration rule in which u(x, y) is approximated as a linear function between points i and i + 1. Analogous formulas can be written down for the other partial derivatives in equation (2). The area A is given by

$$A = \frac{1}{2} \sum_{i=1}^{n} (x_i y_{i+1} - y_i x_{i+1}).$$

[47] **Acknowledgments.** We wish to thank S. S. Pang for her software support during the preparation of this paper. The RGPS data are provided by the Jet Propulsion Laboratory and the Alaska Satellite Facility through a project sponsored by the NASA Earth Science REASoN Program (data are available at http://www-radar.jpl.nasa.gov/rgps/radarsat.html). E. Hunke is supported by the Climate Change Prediction Program of the Department of Energy's Office of Biological and Environmental Research. J. Zhang is supported by NSF (grants ARC0629326, ARC0629312, and ARC0611967) and NASA (grants NNG04GB03G and NNG04GH52G). The NPS contribution has been funded through grants from the National Aeronautics and Space Administration, Department of Energy, and National Science Foundation. Computer resources for the NPS work are provided by the Arctic Region Supercomputing Center under the Department of Defense High Performance Computer Modernization Program. The ECCO2 products are provided by the consortium for Estimating the Circulation and Climate of the Ocean, Phase II (ECCO2 data are available at http://ecco2.org/). The ECCO2 project is sponsored by the NASA Modeling Analysis and Prediction (MAP) program. R. Kwok and D. Menemenlis carried out this work at the Jet Propulsion Laboratory, California Institute of Technology under contract with the National Aeronautics and Space Administration.

References

Adcroft, A. J., J.-M. Campin, C. N. Hill, and J. Marshall (2004), Implementation of an atmosphere-ocean general circulation model on the expanded spherical cube, *Mon. Weather Rev.*, *132*, 2845–2863, doi:10.1175/MWR2823.1.

Babko, O., D. A. Rothrock, and G. A. Maykut (2002), Role of rafting in the mechanical redistribution of sea ice thickness, *J. Geophys. Res.*, *107*(C8), 3113, doi:10.1029/1999JC000190.

Bitz, C. M., and W. H. Lipscomb (1999), An energy-conserving thermodynamic sea ice model for climate study, *J. Geophys. Res.*, *104*, 15,669–15,677, doi:10.1029/1999JC900100.

Collins, W. D., et al. (2006), The Community Climate System Model Version 3 (CCSM3), *J. Clim.*, *19*, 2122–2161, doi:10.1175/JCLI3761.1.

Conkright, M. E., H. E. Garcia, T. D. O'Brien, R. A. Locarnini, T. P. Boyer, C. Stephens, and J. I. Antonov (2002), *World Ocean Atlas 2001*, vol. 4, *Nutrients*, *NOAA Atlas NESDIS*, vol. 52, NOAA, Silver Spring, Md.

Coon, M. D., G. S. Knoke, D. C. Echert, and R. S. Pritchard (1998), The architecture of an anisotropic elastic-plastic sea ice mechanics constitutive law, *J. Geophys. Res.*, *103*, 21,915–21,925, doi:10.1029/98JC01259.

Coon, M., R. Kwok, G. Levy, M. Pruis, H. Schreyer, and D. Sulsky (2007), Arctic Ice Dynamics Joint Experiment (AIDJEX) assumptions revisited and found inadequate, *J. Geophys. Res.*, *112*, C11S90, doi:10.1029/2005JC003393.

Curry, J. A., J. L. Schramm, D. K. Perovich, and J. O. Pinto (2001), Applications of SHEBA/FIRE data to evaluation of snow/ice albedo parameterizations, *J. Geophys. Res.*, *106*, 15,345–15,355, doi:10.1029/2000JD900311.

Dukowicz, J. K., and R. D. Smith (1994), Implicit free-surface for the Bryan-Cox-Semtner ocean model, *J. Geophys. Res.*, *99*, 7991–8014, doi:10.1029/93JC03455.

Fox-Kemper, B., and D. Menemenlis (2008), Can large eddy simulation techniques improve mesoscale rich ocean models?, in *Ocean Modeling in an Eddying Regime*, *Geophys. Monogr. Ser.*, vol. 177, edited by M. Hecht and H. Hasumi, pp. 319–338, AGU, Washington D.C.

Hibler, W. D., III (1979), A dynamic thermodynamic sea ice model, *J. Phys. Oceanogr.*, *9*, 815–846, doi:10.1175/1520-0485(1979)009<0815:ADTSIM>2.0.CO;2.

Hibler, W. D., III (1980), Modeling a variable thickness sea ice cover, *Mon. Weather Rev.*, *108*, 1943–1973, doi:10.1175/1520-0493(1980)108<1943:MAVTSI>2.0.CO;2.

Hibler, W. D., III (2001), Modeling the formation and evolution of oriented fractures in sea ice, *Ann. Glaciol.*, *33*, 157–164, doi:10.3189/172756401781818680.

Hibler, W. D., III, and E. M. Schulson (2000), On modeling the anisotropic failure of flawed sea ice, *J. Geophys. Res.*, *105*, 17,105–17,120, doi:10.1029/2000JC900045.

Hopkins, M. A., J. Tuhkuri, and M. Lensu (1999), Rafting and ridging of ice sheets, *J. Geophys. Res.*, *104*, 13,605–13,613, doi:10.1029/1999JC900031.

Hunke, E. C., and J. K. Dukowicz (2002), The elastic-viscous-plastic sea ice dynamics model in general orthogonal curvilinear coordinates on a sphere — Effect of metric terms, *Mon. Weather Rev.*, *130*, 1848–1865, doi:10.1175/1520-0493(2002)130<1848:TEVPSI>2.0.CO;2.

Hunke, E. C., and M. M. Holland (2007), Global atmospheric forcing data for Arctic ice-ocean modeling, *J. Geophys. Res.*, *112*, C04S14, doi:10.1029/2006JC003640.

Hunke, E. C., and W. H. Lipscomb (2006), CICE: The Los Alamos sea ice model, documentation and software, *Tech. Rep. LA-CC-98–16*, Los Alamos Natl. Lab., Los Alamos, N. M. (http://climate.lanl.gov/Models/CICE/index.htm).

Hutchings, J. K., P. Heil, and W. D. Hibler III (2005), Modelling linear kinematic features in sea ice, *Mon. Weather Rev.*, *133*, 3481–3497, doi:10.1175/MWR3045.1.

Kistler, R., et al. (2001), The NCEP-NCAR 50-year reanalysis: Monthly means CD-ROM and documentation, *Bull. Am. Meteorol. Soc.*, *82*, 247–267, doi:10.1175/1520-0477(2001)082<0247:TNNYRM>2.3.CO;2.

Kwok, R. (1998), The RADARSAT Geophysical Processor System, in *Analysis of SAR Data of the Polar Oceans: Recent Advances*, edited by C. Tsatsoulis and R. Kwok, pp. 235–257, Springer, New York.

Kwok, R., and M. D. Coon (2006), Introduction to special section: Small-scale sea ice kinematics and dynamics, *J. Geophys. Res.*, *111*, C11S21, doi:10.1029/2006JC003877.

Kwok, R., and G. F. Cunningham (2002), Seasonal ice area and volume production of the Arctic Ocean: November 1996 through April 1997, *J. Geophys. Res.*, *107*(C10), 8038, doi:10.1029/2000JC000469.

Kwok, R., and D. A. Rothrock (1999), Variability of Fram Strait flux and North Atlantic oscillation, *J. Geophys. Res.*, *104*, 5177–5189, doi:10.1029/1998JC900103.

Kwok, R., D. A. Rothrock, H. L. Stern, and G. F. Cunningham (1995), Determination of the age distribution of sea ice from Lagrangian observations of ice motion, *IEEE Trans. Geosci. Remote Sens.*, *33*, 392–400, doi:10.1109/36.377939.

Kwok, R., A. Schweiger, D. A. Rothrock, S. Pang, and C. Kottmeier (1998), Sea ice motion from satellite passive microwave data assessed with ERS SAR and buoy data, *J. Geophys. Res.*, *103*, 8191–8214, doi:10.1029/97JC03334.

Kwok, R., G. F. Cunningham, and S. S. Pang (2004), Fram Strait sea ice outflow, *J. Geophys. Res.*, *109*, C01009, doi:10.1029/2003JC001785.

Large, W. G., and A. J. G. Nurser (2001), Ocean surface water mass transformation, in *Ocean Circulation and Climate*, edited by G. Siedler, J. Church, and J. Gould, pp. 317–336, Elsevier, San Diego, Calif.

Large, W. G., and S. Pond (1981), Open ocean momentum flux measurements in moderate to strong winds, *J. Phys. Oceanogr.*, *11*, 324–336, doi:10.1175/1520-0485(1981)011<0324:OOMFMI>2.0.CO;2.

Large, W. G., and S. Pond (1982), Sensible and latent heat flux measurement over the ocean, *J. Phys. Oceanogr.*, *12*, 464–482, doi:10.1175/1520-0485(1982)012<0464:SALHFM>2.0.CO;2.

Large, W., and S. Yeager (2004), Diurnal to decadal global forcing for ocean and sea-ice models: The data sets and flux climatologies, *Tech.*

Note NCAR/TN-460+STR, Clim. and Global Dyn. Div., Natl. Cent. for Atmos. Res., Boulder, Colo.

Lindsay, R. W. (2002), Ice deformation near SHEBA, *J. Geophys. Res.*, *107*(C10), 8042, doi:10.1029/2000JC000445.

Lindsay, R. W. (2003), Changes in the modeled ice thickness distribution near the SHEBA drifting ice camp, *J. Geophys. Res.*, *108*(C6), 3194, doi:10.1029/2001JC000805.

Lindsay, R. W., and H. Stern (2003), The RADARSAT Geophysical Processor System: Quality of sea ice trajectory and deformation estimates, *J. Atmos. Oceanic Technol.*, *20*, 1333–1347.

Lindsay, R. W., and J. Zhang (2006), Assimilation of ice concentration in an ice-ocean model, *J. Atmos. Oceanic Technol.*, *23*, 742–749, doi:10.1175/JTECH1871.1.

Lindsay, R. W., J. Zhang, and D. A. Rothrock (2003), Sea-ice deformation rates from satellite measurements and in a model, *Atmos. Ocean*, *41*(1), 35–47, doi:10.3137/ao.410103.

Lipscomb, W. H. (2001), Remapping the thickness distribution in sea ice models, *J. Geophys. Res.*, *106*, 13,989–14,000, doi:10.1029/2000JC000518.

Lipscomb, W. H., and E. C. Hunke (2004), Modeling sea ice transport using incremental remapping, *Mon. Weather Rev.*, *132*, 1341–1354, doi:10.1175/1520-0493(2004)132<1341:MSITUI>2.0.CO;2.

Lipscomb, W. H., E. C. Hunke, W. Maslowski, and J. Jakacki (2007), Ridging, strength and stability in high-resolution sea ice models, *J. Geophys. Res.*, *112*, C03S91, doi:10.1029/2005JC003355.

Marshall, J., A. Adcroft, C. Hill, L. Perelman, and C. Heisey (1997), A finite-volume, incompressible Navier-Stokes model for studies of the ocean on parallel computers, *J. Geophys. Res.*, *102*, 5753–5766, doi:10.1029/96JC02775.

Martin, T., and R. Gerdes (2007), Sea ice drift variability in Arctic Ocean Model Intercomparison Project models and observations, *J. Geophys. Res.*, *112*, C04S10, doi:10.1029/2006JC003617.

Maslowski, W., and W. H. Lipscomb (2003), High resolution simulations of Arctic sea ice: 1979–1993, *Polar Res.*, *22*(1), 67–74, doi:10.1111/j.1751-8369.2003.tb00097.x.

Maslowski, W., D. Marble, W. Walczowski, U. Schauer, J. L. Clement, and A. J. Semtner (2004), On climatological mass, heat, and salt transports through the Barents Sea and Fram Strait from a pan-Arctic coupled ice-ocean model simulation, *J. Geophys. Res.*, *109*, C03032, doi:10.1029/2001JC001039.

Maslowski, W., J. L. Clement, and J. Jakacki (2007), Towards prediction of environmental change, *Comput. Sci. Eng.*, *9*(6), 29–34, doi:10.1109/MCSE.2007.125.

Maykut, G. A. (1986), The surface heat and mass balance, in *Geophysics of Sea Ice*, *NATO ASI Ser., Ser. B*, vol. 146, edited by N. Untersteiner, pp. 395–463, Springer, New York.

Meier, W. N., and J. A. Maslanik (2003), Effect of environmental conditions on observed, modeled, and assimilated sea ice motion errors, *J. Geophys. Res.*, *108*(C5), 3152, doi:10.1029/2002JC001333.

Menemenlis, D., et al. (2005), NASA supercomputer improves prospects for ocean climate research, *Eos Trans. AGU*, *86*(9), 89, doi:10.1029/2005EO090002.

Parmerter, R. R., and M. Coon (1972), Model of pressure ridge formation in sea ice, *J. Geophys. Res.*, *77*, 6565–6575, doi:10.1029/JC077i033p06565.

Paulson, C. A., and J. J. Simpson (1977), Irradiance measurements in the upper ocean, *J. Phys. Oceanogr.*, *7*, 952–956, doi:10.1175/1520-0485(1977)007<0952:IMITUO>2.0.CO;2.

Richter-Menge, J. A., S. L. McNutt, J. E. Overland, and R. Kwok (2002), Relating arctic pack ice stress and deformation under winter conditions, *J. Geophys. Res.*, *107*(C10), 8040, doi:10.1029/2000JC000477.

Rothrock, D. A. (1975), The energetics of the plastic deformation of pack ice by ridging, *J. Geophys. Res.*, *80*, 4514–4519, doi:10.1029/JC080i033p04514.

Stroeve, J., and W. Maslowski (2007), Arctic sea ice variability during the last half century, in *Climate Variability and Extremes During the Past 100 Years*, vol. 33, *Advances in Global Change Research*, edited by S. Bronnimann et al., pp. 143–154, Springer, New York.

Thorndike, A. S., and R. Colony (1982), Sea ice motion in response to geostrophic winds, *J. Geophys. Res.*, *87*, 5845–5852, doi:10.1029/JC087iC08p05845.

Thorndike, A. S., D. A. Rothrock, G. A. Maykut, and R. Colony (1975), The thickness distribution of sea ice, *J. Geophys. Res.*, *80*, 4501–4513, doi:10.1029/JC080i033p04501.

Zhang, J. (2007), Increasing Antarctic sea ice under warming atmospheric and oceanic conditions, *J. Clim.*, *20*, 2515–2529, doi:10.1175/JCLI4136.1.

Zhang, J., and W. D. Hibler (1997), On an efficient numerical method for modeling sea ice dynamics, *J. Geophys. Res.*, *102*, 8691–8702, doi:10.1029/96JC03744.

Zhang, J., and D. A. Rothrock (2001), A thickness and enthalpy distribution sea-ice model, *J. Phys. Oceanogr.*, *31*, 2986–3001, doi:10.1175/1520-0485(2001)031<2986:ATAEDS>2.0.CO;2.

Zhang, J., and D. A. Rothrock (2003), Modeling global sea ice with a thickness and enthalpy distribution model in generalized curvilinear coordinates, *Mon. Weather Rev.*, *131*, 845–861, doi:10.1175/1520-0493(2003)131<0845:MGSIWA>2.0.CO;2.

Zhang, J., and D. A. Rothrock (2005), The effect of sea-ice rheology in numerical investigations of climate, *J. Geophys. Res.*, *110*, C08014, doi:10.1029/2004JC002599.

Zhang, J., W. Hibler, M. Steele, and D. Rothrock (1998), Arctic ice-ocean modeling with and without climate restoring, *J. Phys. Oceanogr.*, *28*, 191–217.

Zhang, J., D. R. Thomas, D. A. Rothrock, R. W. Lindsay, Y. Yu, and R. Kwok (2003), Assimilation of ice motion observations and comparisons with submarine ice thickness data, *J. Geophys. Res.*, *108*(C6), 3170, doi:10.1029/2001JC001041.

Zhang, Y., W. Maslowski, and A. J. Semtner (1999), Impacts of mesoscale ocean currents on sea ice in high-resolution Arctic ice and ocean simulations, *J. Geophys. Res.*, *104*, 18,409–18,429, doi:10.1029/1999JC900158.

E. C. Hunke, Climate, Ocean, and Sea Ice Modeling Program, Los Alamos National Laboratory, P.O. Box 1663, Los Alamos, NM 87545, USA.

R. Kwok and D. Menemenlis, Jet Propulsion Laboratory, California Institute of Technology, 4800 Oak Grove Drive, Pasadena, CA 91109, USA. (ron.kwok@jpl.nasa.gov)

W. Maslowski, Department of Oceanography, Graduate School of Engineering and Applied Sciences, Naval Postgraduate School, Monterey, CA 93943, USA.

J. Zhang, Polar Science Center, Applied Physics Laboratory, College of Ocean and Fishery Sciences, University of Washington, Seattle, WA 98105, USA.